The Imaging Magnetograph eXperiment (IMaX) for the *Sunrise* Balloon-Borne Solar Observatory

V. Martínez Pillet · J.C. del Toro Iniesta · A. Álvarez-Herrero · V. Domingo ·
J.A. Bonet · L. González Fernández · A. López Jiménez · C. Pastor ·
J.L. Gasent Blesa · P. Mellado · J. Piqueras · B. Aparicio · M. Balaguer ·
E. Ballesteros · T. Belenguer · L.R. Bellot Rubio · T. Berkefeld · M. Collados ·
W. Deutsch · A. Feller · F. Girela · B. Grauf · R.L. Heredero · M. Herranz ·
J.M. Jerónimo · H. Laguna · R. Meller · M. Menéndez · R. Morales ·
D. Orozco Suárez · G. Ramos · M. Reina · J.L. Ramos · P. Rodríguez · A. Sánchez ·
N. Uribe-Patarroyo · P. Barthol · A. Gandorfer · M. Knoelker · W. Schmidt ·
S.K. Solanki · S. Vargas Domínguez

Abstract The Imaging Magnetograph eXperiment (IMaX) is a spectropolarimeter built by
four institutions in Spain that flew on board the *Sunrise* balloon-borne solar observatory
in June 2009 for almost six days over the Arctic Circle. As a polarimeter, IMaX uses fast
polarization modulation (based on the use of two liquid crystal retarders), real-time im-
age accumulation, and dual-beam polarimetry to reach polarization sensitivities of 0.1%.
As a spectrograph, the instrument uses a LiNbO$_3$ etalon in double pass and a narrow band

V. Martínez Pillet (✉) · J.A. Bonet · E. Ballesteros · M. Collados · S. Vargas Domínguez
Instituto de Astrofísica de Canarias, 38200, La Laguna, Tenerife, Spain
e-mail: vmp@iac.es

J.C. del Toro Iniesta · A. López Jiménez · P. Mellado · B. Aparicio · M. Balaguer · L.R. Bellot Rubio ·
F. Girela · M. Herranz · J.M. Jerónimo · R. Morales · D. Orozco Suárez · J.L. Ramos
Instituto de Astrofísica de Andalucía (CSIC), Apdo. de Correos 3004, 18080, Granada, Spain

A. Álvarez-Herrero · L. González Fernández · C. Pastor · T. Belenguer · R.L. Heredero · H. Laguna ·
M. Menéndez · G. Ramos · M. Reina · A. Sánchez · N. Uribe-Patarroyo
Instituto Nacional de Técnica Aeroespacial, 28850, Torrejón de Ardoz, Madrid, Spain

V. Domingo · J.L. Gasent Blesa · P. Rodríguez
Grupo de Astronomía y Ciencias del Espacio, Univ. de Valencia, 46980, Paterna, Valencia, Spain

J. Piqueras · W. Deutsch · A. Feller · B. Grauf · R. Meller · P. Barthol · A. Gandorfer · S.K. Solanki
Max-Planck-Institut für Sonnensystemforschung, 37191, Katlenburg-Lindau, Germany

T. Berkefeld · W. Schmidt
Kiepenheuer-Institut für Sonnenphysik, 79104, Freiburg, Germany

M. Knoelker
High Altitude Observatory (NCAR), 80307-3000, Boulder, USA

pre-filter to achieve a spectral resolution of 85 mÅ. IMaX uses the high-Zeeman-sensitive line of Fe I at 5250.2 Å and observes all four Stokes parameters at various points inside the spectral line. This allows vector magnetograms, Dopplergrams, and intensity frames to be produced that, after reconstruction, reach spatial resolutions in the $0.15 - 0.18$ arcsec range over a 50×50 arcsec field of view. Time cadences vary between 10 and 33 s, although the shortest one only includes longitudinal polarimetry. The spectral line is sampled in various ways depending on the applied observing mode, from just two points inside the line to 11 of them. All observing modes include one extra wavelength point in the nearby continuum. Gauss equivalent sensitivities are 4 G for longitudinal fields and 80 G for transverse fields per wavelength sample. The line-of-sight velocities are estimated with statistical errors of the order of $5 - 40$ m s^{-1}. The design, calibration, and integration phases of the instrument, together with the implemented data reduction scheme, are described in some detail.

1. Introduction

Increasing our understanding of solar magnetism poses high demands on spatial resolution and polarimetric sensitivity. One-meter aperture telescopes allow solar structures with typical sizes of about 100 km (in the visible) to be resolved, which has proven very beneficial in identifying fundamental ingredients of active region plages, penumbral filaments, umbral dots, and solar granulation (Scharmer, 2009; Lites *et al.*, 2004). The requirements for the detectability of the (often weak) magnetic fields that interact with the plasma at the solar surface are very stringent. Recent magnetoconvection simulations of the conditions in the quiet Sun show distributions of field strengths that increase monotonically from the kG fields to values of about 1 G (gauss) as shown by, *e.g.*, Pietarila Graham *et al.* (2009). 1 G of longitudinal field produces a polarization signal that requires the detection of $4800^2 \approx 2 \cdot 10^7$ photoelectrons in a time scale short enough for this field not to evolve considerably (seconds). This is a very demanding measurement. For transverse fields of a similar magnitude, the situation is much more discouraging, as one needs now to detect $2500^4 \approx 4 \cdot 10^{13}$ photoelectrons (the rationale for these numbers is given in Section 9.3). It is in this context that a number of solar physics projects have been conceived in the last decade for the construction of large-aperture telescopes and high sensitivity polarimeters, both ground-based (4-m class telescopes; see Rimmele *et al.* (2009) and Collados (2009)) and space-borne (*Hinode*, Kosugi, 2007). Led by the Max Planck Institut für Sonnensystemforschung (MPS, Katlenburg-Lindau, Germany), the *Sunrise* project (Barthol *et al.*, 2010) is a multi-national effort of that type aimed at imaging the near-UV continuum and at observing the photospheric magnetic field and velocity from a balloon platform with a 1-m aperture telescope. To this end *Sunrise* uses the Imaging Magnetograph eXperiment (IMaX) to map the line-of-sight (LOS) velocity and the complete magnetic field vector using spectropolarimetric observations of a photospheric line.

IMaX has been designed, built, and calibrated by a consortium of four institutions in Spain. The Instituto de Astrofísica de Canarias (IAC, Tenerife) is the leading institution and

Figure 1 Top: IMaX optical enclosure just after integration and verification at INTA. The top cover (a radiator) is not in place yet. Labels correspond to the pre-filter and LCVR mounting, the LiNbO$_3$ etalon enclosure, the polarizing beamsplitter, the CCDs, the heat pipes, and the proximity electronics enclosure in the lower left. Bottom: IMaX main electronic enclosure. Labels correspond to the control computer and real-time electronics (DPU), the DC/DC converters, the heat pipes, the fan, the interface board, and the thermal controllers.
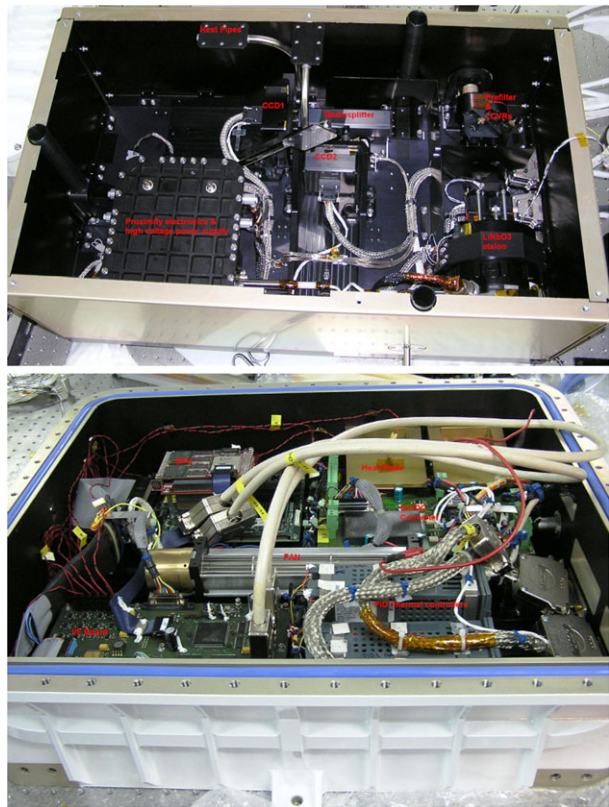
has been in charge of the conceptual design, management of the consortium, and the ground-based control software. The Instituto de Astrofísica de Andalucía (IAA – CSIC, Granada) has been in charge of all the electronic aspects of the instrument. These include the detectors, real-time electronics, control computer and software, power supply and distribution, and harness. The Instituto Nacional de Técnica Aeroespacial (INTA, Torrejón de Ardoz) has developed the optical definition of the instrument, its opto-mechanical concept, and the thermal sub-system. The Grupo de Astronomía y Ciencias del Espacio (GACE, Valencia) has provided the three enclosures (two of them pressurized) used by the instrument. The Assembly, Integration and Verification (AIV) of the instrument (and various sub-systems) has been performed at INTA facilities prior to the submission of the instrument to MPS. A conceptual description of the instrument has been provided elsewhere (Martínez Pillet *et al.*, 2004). The description presented there is still valid with the exception of the spectral line used by the instrument at that time, the detectors, and the pre-filter bandpass. The status of the project at the critical design stage can be found in Álvarez-Herrero *et al.* (2006a). An illustration of the instrument is shown in Figure 1. The top panel shows the Optical Bench Enclosure (OBE) and the bottom one is a picture of the Main Electronics Enclosure (MEE). The black anodized box inside the OBE is the Proximity Electronics Enclosure (PEE).

This paper describes the IMaX instrument in detail, from the conceptual level to the complete calibration process at INTA facilities, at MPS facilities, and in the launch field of the ESRANGE Space Center (Kiruna, Sweden). IMaX data reduction and calibration is

also covered in some detail. The paper is intended to contain all the information needed for analysing the data obtained by the instrument during the June 2009 flight.

2. Instrument Concept

2.1. Instrument Requirements

To accomplish its scientific objectives, IMaX must perform near diffraction-limited imaging with high spectroscopic resolving power and very high sensitivity polarimetry. Differential imaging in selected wavelengths of a Zeeman-sensitive spectral line is needed to extract the necessary information to infer the vector magnetic field and the LOS velocity of the solar plasma. These three characteristics were borne in mind during the entire design, development, and construction phases of the instrument. Extensive prior studies had to be carried out in order to select the minimum performance of the instrument, and a significant number of trade-offs have been taken into account.

First of all, IMaX had to preserve the imaging capabilities of the *Sunrise* 1-m telescope to the maximum. The system-level specification for the image quality of IMaX was set independently of the rest of the optical setup in front of the instrument (ISLiD and telescope, Gandorfer *et al.*, 2010).[1] It has been given in terms of the Strehl ratio that the instrument should have for an aberration-free image at F4 (the nominal entrance focus of IMaX and the interface with the ISLiD). It requires that the Strehl ratio in the IMaX image plane be better than 0.9 for nominal optical configuration and that the effect of fabrication and alignment tolerances not degrade the Strehl ratio to less than 0.8 ($\lambda/14$) over the entire field of view (FOV). This requirement was set after confirmation of the high optical quality achievable by the etalon as stated by the manufacturer. Several factors can deteriorate the image quality, such as internal aberrations due to misalignments or poor optical quality of the IMaX components and errors induced from residual jittering of the platform among others. To guarantee a good recovery of near-diffraction images, we decided to use a phase diversity mechanism to evaluate the point spread function (PSF) of the instrument right after every observing run, so that the observed images can be deconvolved from this PSF. Extensive calculations (Vargas Domínguez, 2009) led us to conclude that an rms wavefront error (WFE) of $\lambda/5$ can be accepted for IMaX in order not to lose spatial resolution after PSF deconvolution.

Second, the spectroscopic and polarimetric capabilities of the instrument, along with the sensitivity of the finally selected spectral line, are intimately involved to ensure the instrument magnetic and kinematic performance. The community has reached a general consensus that a minimum signal-to-noise ratio (S/N) of 10^3 is required to detect the weak polarization signals present in the internetwork part of the quiet Sun (although higher values are desirable). S/N is the key parameter governing the photometric and polarimetric sensitivity of the instrument since it yields the minimum intensity, δI, and minimum polarization degree, δp with p the polarization degree itself, that can be detected:[2]

$$\frac{\delta I}{I} = \frac{1}{\text{S/N}}; \qquad \frac{\delta p}{p} \geq \frac{\sqrt{1+3/p^2}}{\text{S/N}}. \tag{1}$$

---

[1]ISLiD is an acronym for Image Stabilization and Light Distribution system.

[2]Note here that S/N is defined as the ratio between a signal at a given wavelength over noise at the same wavelength, whereas the common use of this figure of merit is computed at continuum wavelengths.

Polarimetric accuracy is usually measured through what are called the polarimetric efficiencies (see Section 2.3.1). The minimum IMaX efficiencies for Stokes Q, U, and V were set to 0.45. Numerical experiments, including synthetic observations built with magnetohydrodynamical simulations (Vögler *et al.*, 2005) of the solar photosphere and analysed with inversions of the radiative transfer equation, were carried out (Orozco Suárez, 2008; Orozco Suárez *et al.*, 2010). These experiments indicated that a spectral resolution of the order of $50 - 100$ mÅ (with a preference for the high resolution range), in four wavelengths across the line profile plus one in the continuum, is enough to achieve accurate values of the vector magnetic field and the LOS velocity from post-processing of the IMaX data.

2.2. Basic Design Concepts for a High Sensitivity Polarimeter

As mentioned in the introduction, the polarimetric sensitivity required to measure 1 G of longitudinal field requires typically 10^7 photoelectrons or so. Currently available charge-coupled devices (CCDs) have full wells of about 10^5 electrons, and in a typical exposure one can only fill a fraction of that. This readily tells us that with single exposures it is impossible to reach these magnetic sensitivities. For this reason modern solar polarimeters introduced image accumulation to add a number, N_A, of single exposures to achieve the desired sensitivity or S/N. This scheme was successfully employed and popularized by the Advanced Stokes Polarimeter (ASP, Elmore, 1992). Other polarimeters that follow this scheme of real-time addition of exposures to achieve a $S/N \approx 10^3$ are the Tenerife Infrared Polarimeter (TIP I and II, Martínez Pillet *et al.*, 1999; Collados *et al.*, 2007); ZIMPOL (Gandorfer *et al*. (2004) and references therein), and the *Hinode*/SP (Lites, Elmore, and Streander, 2001). Accumulation, but used after applying reconstruction techniques (speckle or blind deconvolution), is also becoming popular in ground-based filter magnetographs (Bello González and Kneer, 2008; Viticchié *et al*., 2009; van Noort and Rouppe van der Voort, 2008).

An additional complication results from the fact that a polarimeter is a differential imager (see Martínez Pillet, 2006). The polarization signals are inferred from the subtraction of two (or more) images, referred to as the polarization modulation images, taken at different times. Any difference between them that originated from atmospheric seeing, pointing errors, or even solar evolution is interpreted as a real polarization signal. There are two complementary ways to minimize this effect, as explained, *e.g.*, by Del Toro Iniesta (2003). First, one implements fast temporal polarization modulation so that the time between the images that will be subsequently subtracted is minimized. This imposes serious requirements on the polarization modulator, which is normally a spinning retarder (as in the ASP or in *Hinode*) or an electro-optical retarder based on some type of liquid crystal material (typically ferroelectric as in TIP or nematic as in IMaX). Slower polarization modulators with step motors (such as in *SOHO*/MDI, Scherrer, 1995) are only viable options at low spatial resolution and with accurate pointing in the absence of atmospheric disturbances. The temporal polarization modulation is then synchronized to the detector readout which typically requires careful selection of the CCD chip and its shutter concept. Second, to minimize jittering-induced spurious signals, one measures the various polarization modulation images in the two orthogonal linear states produced by a polarizing beamsplitter (as originally proposed by Lites (1987); sometimes also referred to as a dual-beam configuration). By combining the images obtained in these two orthogonal states, one not only makes use of all the available photons, but also cancels out, to first order, the fluctuations produced by Stokes I to the other Stokes parameters due to image motion or solar evolution. The combination of these three properties, image accumulation to increase S/N, rapid polarization modulation, and dual-beam configuration, is at the core of all modern high sensitivity polarimeters (such as the *Hinode*/SP instrument). IMaX also uses these three properties. While

Table 1 IMaX requirements and performance.

Wavelength	5250.2 Å
Spectral resolution $\delta\lambda$	65 mÅ (85 mÅ Gaussian)
Spatial sampling	0.055 arcsec pixel^{-1}
Focal depth at F4	± 0.66 mm
Lateral magnification	1.8
Image quality (only IMaX)	Strehl 0.7 ($\lambda/11$)
Image quality (in flight)	Strehl 0.3 $\lambda/5.4$
N_λ (number of wavelengths)	2, 4, 11 + continuum
N_p (number of Stokes parameters)	2, 4
N_A (number of image accumulations)	variable, 6 for $N_p = 4$, $N_\lambda = 5$
t_{ex} (individual exposures)	246 ms
Field of view	$\approx 50 \times 50$ arcsec
Wavelength drift over FOV	≈ 28 mÅ
(S/N)$_i$ (photon noise)	850 – 1000 (5 G B_L, 80 G B_T)
Exp. time for $N_\lambda = 5$, $N_p = 4$, $N_A = 6$	33 s
Exp. time for $N_\lambda = 1$, $N_p = 4$, $N_A = 6$	6 s
OBE weight	49.0 kg
EE weight	26.7 kg
Power	191/234 W (mean/peak)
Data rate	996 kB s^{-1}

in the case of *Hinode*/SP the pointing of the platform and the excellent performance of the on-board correlation tracker (Shimizu *et al.*, 2008) have made the use of the two orthogonal states measured by the SP less relevant (Lites, private communication), the expected pointing errors from a balloon gondola suggested its implementation. Indeed, early in the project we used the pointing errors published by the Flare Genesis Experiment (FGE, Bernasconi *et al.*, 2000) to simulate the spurious polarization signals introduced by them. More specifically, a single camera with an image jittering of 5 arcsec rms and a white noise spectrum for frequencies up to 10 Hz was used (see Figure 3 in Bernasconi *et al.*, 2000). The residual motions were partially compensated by a standard attenuation curve of a typical correlation tracker. An image of the granulation was then subjected to such residual jitter, and the differences between the consecutive displaced frames analysed. This test showed that the expected level of spurious polarization signal was 10^{-2}, an order of magnitude larger than the intended polarimetric sensitivity, hence proving the need for a dual-beam polarimeter in IMaX.

The performance of the instrument during its 2009 flight is detailed in Table 1.

2.3. Functional Concept and Trade-offs

Solar magnetographs must be capable of doing polarimetry, spectroscopy, and imaging with the highest possible quality. These three different capabilities make them necessarily complex instruments. IMaX selected the well-known spectral line of Fe I at 5250.2 Å ($g = 3$, $\chi_i = 0.121$ eV) as being the highest Zeeman sensitivity line in the green part of the spectrum.

2.3.1. Polarimetry

In the different observing modes of the instrument, a single exposure shot corresponds to one of the polarization modulation states out of the N_p being used by the instrument in this mode and to one specific wavelength out of the N_λ being observed. Of these individual exposures, IMaX real-time electronics adds N_A of them to produce one single final image. If the exposure time of a single shot is t_{ex}, then the total time used to observe all polarization states in all wavelength points is clearly $N_A N_p N_\lambda t_{ex}$. The observations made at continuum wavelength have an effective exposure time of $N_A N_p t_{ex}$.

For the polarization analysis, IMaX uses two custom nematic liquid crystal variable retarders (LCVRs) and a commercial polarizing beamsplitter. The optical axis of the first LCVR (as seen by the light entering IMaX) is oriented parallel to one of the linear polarization directions of the beamsplitter. The second LCVR's optical axis is oriented at 45° relative to this direction. Polarization modulation is achieved by driving the LCVRs with specific sets of voltages. This combination of two LCVRs is very efficient in producing either four linearly independent modulation states $[I_1, I_2, I_3, I_4]$ ($N_p = 4$) for vector polarimetry or two modulation states providing the canonical combination of $I + V$ and $I - V$ for longitudinal polarimetry ($N_p = 2$). This flexibility is very specific of LCVRs and cannot be found in modulators based on rotating waveplates or on ferroelectric liquid crystals (Martínez Pillet *et al.*, 2004). In the case of vector polarimetry, the modulation states are related to the Stokes vector ($[S_1, S_2, S_3, S_4] = [I, Q, U, V]$) by the modulation matrix **M**:

$$I_i = \sum_{j=1}^{4} M_{ij} S_j, \quad i = 1, 2, 3, 4, \tag{2}$$

with the demodulation matrix (that needed to deduce the Stokes parameters from the measurements) being simply $\mathbf{D} = \mathbf{M}^{-1}$. The coefficients of **D** are used in turn to estimate the polarimetric efficiencies:

$$\epsilon_i = \left(N_p \sum_{j=1}^{4} D_{ij}^2 \right)^{-1/2}, \quad i = 1, 2, 3, 4. \tag{3}$$

If a modulation scheme weights Q, U, and V equally, and a combination of LCVR voltages is found that maximizes the S/N, then $\epsilon_{2,3,4}$ are known to reach a maximum value of $1/\sqrt{3}$. $\epsilon_{1,max} = 1$. The derivation of these properties is conveniently explained in Del Toro Iniesta and Collados (2000). With these definitions, the signal-to-noise ratio of the accumulated image in each Stokes parameter $(S/N)_i$ from each individual camera can be derived to be

$$(S/N)_i = (s/n) \, \epsilon_i \sqrt{N_p N_A}, \quad i = 1, 2, 3, 4, \tag{4}$$

with (s/n) being the signal-to-noise ratio of the individual exposures (integrated for t_{ex} seconds; Martínez Pillet *et al.*, 1999).

The polarization analysis is made by a polarizing beamsplitter near the CCD cameras. In between the LCVRs and the beamsplitter there are several optical elements, including lenses, three folding mirrors, and the etalon. While the LCVRs change state, these optical elements remain constant and thus induce no variation of the polarimetric efficiencies compared to the case when the beamsplitter is located right after the LCVRs. However, the actual coefficients of the modulation matrix **M** do depend on the actual polarization properties of these optical elements.

2.3.2. *Spectroscopy*

For the spectral analysis, IMaX uses a combination of two optical systems: a 1 Å full width at half-maximum (FWHM) pre-filter and a double-pass LiNbO$_3$ etalon. While these etalons have already been used in the past in solar astronomy (in the FGE balloon in particular, Bernasconi *et al.*, 2000), the concept used in IMaX is novel. The rationale of the IMaX spectroscopic concept is as follows. According to Section 2.1, the instrument had to achieve a spectral resolution $\delta\lambda = 50 - 100$ mÅ. The choice of the LiNbO$_3$ etalon technology (developed by ACPO, Australian Center for Precision Optics, CSIRO) was also clear from the beginning. By comparison, the more common technology used in ground-based instruments of piezo-stabilized etalons (TESOS: Kentischer *et al.*, 1998; GFPI: Puschmann *et al.*, 2006; and CRISP: Scharmer *et al.*, 2008) poses serious demands in terms of weight of the instrument and in-flight calibration, such as the need for calibrating plate parallelism and system finesses autonomously. Solid etalons based on man-made LiNbO$_3$ crystals are comparatively weightless and their calibration much easier (see Section 8.4). The weight requirements of this technology are driven by the pressurized enclosure (common to piezo etalons) and by the high voltage needed to change the refractive index of the crystal and tune between different wavelengths. A High Voltage Power Supply (HVPS) working in the range of ± 5000 V has been employed (see Section 5.2). Additionally, the relatively high refractive index of this material ($n \approx 2.3$) permits incidence angles over the etalon n times larger than their piezo-controlled counterparts, thus allowing for smaller etalon sizes and more compact instruments.

LiNbO$_3$ etalons can be fabricated with thicknesses of 200 μm, or larger, and with a reflectivity (R) high enough to permit resolving powers of 50 mÅ, as required, using just a single etalon. However, their fabrication finesse (F_f, for a definition, see Atherton *et al.*, 1982) is hardly better than 30 over an aperture of 6 cm (Arkwright *et al.*, 2005). As is well known (Atherton *et al.*, 1982), it is convenient to use reflective finesses F_r for the etalons similar to the fabrication finesse, which combined provide a total finesse F in the range $20 - 25$ ($F^{-2} = F_f^{-2} + F_r^{-2}$). The total finesse of the etalon, its resolving power, and the free spectral range (FSR) are related to each other by

$$F = \frac{\text{FSR}}{\delta\lambda}. \tag{5}$$

Now, with $F = 22$ (the value for the IMaX etalon) and $\delta\lambda = 50$ mÅ, the FSR is about 1 Å. Thus, to filter out nearby etalon orders, a pre-filter with at least 0.5 Å is needed or, in its absence, a second etalon. None of these solutions is practical, as the smallest pre-filters available in the market have an FWHM of 1 Å and a second etalon requires a second HVPS which would add considerable extra complexity to the instrument. Instead, the solution adopted was to ask for an etalon with $\delta\lambda = 100$ mÅ and have the light pass through it twice (decreasing the FWHM by a factor $\sqrt{2}$). In this case, the FSR of the etalon is raised to about 2 Å and a pre-filter with 1 Å FWHM can conveniently suppress the extra etalon orders. In this way, a simplified instrument capable of achieving the required resolving power, but still using only one etalon, was defined. The exact properties of the pre-filter and etalon are presented in detail below.

The exact location of an etalon in a magnetograph is to some extent a matter of taste. The two options commonly used are to place the etalon near a telecentric focal plane (TESOS, Kentischer *et al.*, 1998; CRISP, Scharmer *et al.*, 2008) or at a pupil plane within the instrument (GFPI, Puschmann *et al.*, 2006; IBIS, Viticchié *et al.*, 2009). The pros and cons of both solutions have been discussed in some detail by von der Lühe and Kentischer (2000),

Gary, Balasubramaniam, and Sigwarth (2003), and Scharmer (2006). Neither of the options is free of complex calibration problems. IMaX selected the collimated configuration mainly because the exact impact of the pupil apodization problem in magnetograms was not well understood when the decision was taken. The success of the CRISP instrument in achieving diffraction-limited snapshots (with the aid of blind deconvolution post-processing) proves that this effect can be adequately controlled during the design phase of a telecentric system. In the case of the collimated configuration, one benefits from a homogeneous instrument profile for all points in the final image, but a wavelength shift across the FOV appears due to the inclination of the off-axis rays as they reach the etalon. This effect is commonly referred to as the wavelength blueshift of the collimated configuration. Its calibration for the IMaX case is explained in Section 9.1.

The biggest concern with an etalon in a collimated configuration is the degradation of the image quality that it can produce. In particular, von der Lühe and Kentischer (2000) derived an equation for the WFE introduced by an etalon near a pupil plane due to the presence of cavity (polishing) errors of a magnitude Δ_{rms} (see their Equation (10)). This formulation predicted that it could be very difficult to reach diffraction-limited performance in the collimated configuration (see also Scharmer, 2006; Martínez Pillet *et al.*, 2004). For a LiNbO$_3$ etalon with $\Delta_{\text{rms}} \approx 1.3$ nm (corresponding to $\mathsf{F}_\text{f} = 30$, the value of the IMaX etalon over the full aperture) and a typical coating reflectivity of 0.97, this equation predicts a wavefront error of $\lambda/5$. Such an optical element alone considerably degrades the image quality of the system. However, the WFE measurements made by ACPO/CSIRO and by us using Zygo interferometers on real etalons (Álvarez-Herrero *et al.*, 2006a) have shown this equation to predict wavefront degradations that are too large. We have found two reasons for these large estimates. First, Scharmer (2006) pointed out that this equation has to be averaged over the transmission profile, and not just applied at the transmission peak (where the wavefront deformation is maximum). Wavefront degradations will be half as large when properly averaged over the transmission profile. Second, and equally important, is the fact that when this equation is computed, one should not use the value of the reflectivity in the etalon coatings. Instead, one should infer an effective reflectivity that accounts for the total finesse (reflective and fabrication) of the etalon and use this value in the equation. That is, define R_{eff} so that

$$\mathsf{F} = \frac{\pi \sqrt{R_{\text{eff}}}}{1 - R_{\text{eff}}} \tag{6}$$

and introduce R_{eff} instead of the coating reflectivity R in the equation of von der Lühe and Kentischer (2000). It is easy to understand why the effective reflectivity gives a better prediction of the actual wavefront deformation. As shown by Atherton *et al.* (1982), the total finesse is the number of effective bounces of the rays that are added coherently by the etalon to produce the interferometric pattern (instead of the theoretical infinite number of bounces). Using an effective reflectivity, which correctly quantifies how many times the wavefront interacts with the etalon surfaces, should produce a more accurate description of the deformation that it suffers. When one does so, in the case of IMaX ($R = 0.9$, $R_{\text{eff}} = 0.867$), the predicted wavefront error is, at the transmission peak, $\lambda/14$ and when averaged over the full bandpass, $\lambda/27$. Measurements by ACPO/CSIRO gave values in the range $\lambda/23 - \lambda/38$ for the two IMaX etalons (flight unit and spare). These values were confirmed at INTA for the spare unit but not for the flight unit, as commented in Section 8.1. In any case, it is clear that diffraction-limited performance with an etalon near a pupil plane is indeed possible if care is taken of the balance between cavity errors and coating reflectivity (for the specific case of IMaX, see Martínez Pillet *et al.* (2004) and Álvarez-Herrero *et al.* (2006b)).

2.3.3. *Imaging*

High spatial resolution was at the forefront in the list of requirements for the definition of the mission and of the instrument. At system level, a wavefront sensor with refocusing capabilities and low order aberration correction was implemented (see Berkefeld *et al.*, 2010). At instrument level, and in order to cope with slow thermal drifts that change the residual aberrations of the instrument, phase diversity (PD) capabilities were included. IMaX uses a thick glass plate that can be moved in front of the CCD camera at a right angle to the beam entering the beamsplitter (and referred to as camera 1; the camera in the same direction as the light entering the beamsplitter is camera 2). This plate is not inserted into the beam in normal observing modes, but after an observing run is completed, the plate is introduced and a burst of 30 images is acquired in the two cameras. These images are observed only at continuum wavelengths and with no modulation implemented in the LCVRs. However, the images are accumulated as in the subsequent observing run to ensure a similar S/N ratio. Post-processing analysis of these images allows the Zernike coefficients describing the optical quality of the complete system to be recovered.

2.4. Light and Data Path

Light reaches IMaX at the F4 focus of the ISLiD. The first element that is encountered is the pre-filter (whose properties are given in Section 3.1). In this way only 1 Å of solar flux enters the instrument, while the rest is directly sent into a light trap. The pre-filter also protects the LCVRs from any residual UV light that might still be present in the beam, although the majority of the UV photons have been directed to the *Sunrise* UV Filter Imager SuFI (Gandorfer *et al.*, 2010). After the pre-filter, light travels through the two LCVRs (Section 3.2), where the light intensity is encoded for the polarization measurements. The pre-filter and the LCVRs share the same opto-mechanical, thermally stabilized mounting. Light then reaches the collimating lenses (the optical design is described in Section 4) and makes the first pass through the $LiNbO_3$ pressurized enclosure (traversing, in this order, a window, the etalon, and a second window). The etalon (Section 3.3) is located inside a thermally stabilized enclosure provided by ACPO/CSIRO that includes two fused silica windows. Two 45° incidence folding mirrors turn the light backwards to enter the etalon enclosure again and make the second pass through it (in a different area of the etalon). An aperture stop (of 25 mm diameter) is at a symmetric position between the two etalon passes. After exiting the etalon enclosure for the second time, light passes through the camera lenses that produce the final image on the focal plane detectors. The collimating and camera lenses share the same opto-mechanical mounting located in front of the etalon. The folding mirrors, at the other side of the etalon enclosure, use a different mechanical mounting. The two housings on either side of the etalon are thermally controlled with a proportional-integral-derivative system (PID; the thermal design is described in Section 6). A third folding mirror (located in the pre-filter and LCVR mounting) sends the light towards the linear polarizing beamsplitter that finally directs the light to the two CCDs (Section 3.4). The motorized PD plate system lies in between the beamsplitter and camera 1. The detectors' readouts are synced with the LCVR states, and the frames are sent to the real-time IMaX electronics (Section 5), where the images are accumulated N_A times. This is repeated at each of the N_λ wavelengths, producing a total of $N_p \times N_\lambda$ images that are then sent to the IMaX on-board control computer. Lossless JPEG-2000 compression is applied to the data, which is then sent to the *Sunrise* ICU (Instrument Control Unit) and to the storage disks. Some of the images can be sent as thumbnails to the ground control computers depending on the available

telemetry and the adopted thumbnail policy. Polarization demodulation was implemented in the on-board software, as demodulated images have better compression factors. However, this option was not used during the flight, as the data storage capacity was never critical.

The LCVRs are tuned while the light is being recorded by the detectors. As their tuning times are finite, the transitions of the LCVR states are integrated by the detectors. The effect of this integration of non-constant LCVR states is fully taken into account by the instrument polarization calibration (described in Section 8.3). Wavelength tuning is slower (see Section 3.3), and while the etalon changes the observed wavelength, the CCDs are being read out, but the frames are discarded.

3. Concept Implementation

3.1. The IMaX Pre-Filter

The availability of ultra-narrow bandpass, high transmission filters from Barr Associates was at the very core of the IMaX instrument definition. Metal oxide optical interference coatings are used in combination with various colored glasses to produce filters with a bandpass of 1 Å and high out-band blocking ratios. Additionally, these pre-filters have been demonstrated to be thermally stable and environmentally robust. The IMaX pre-filters (flight and spare units) were taken to the French-Italian THEMIS telescope at Teide Observatory for calibration. The bandpass was accurately measured at the nominal temperature and is shown in Figure 2. The properties of the flight unit are given in Table 2. These measurements quantified three crucial aspects for the correct functioning of IMaX: the 1 Å bandpass, a high transmission, and the sensitivity angle. As usual, the pre-filter was ordered slightly shifted to the blue of the nominal working wavelength; in particular, at $5250.65 + 0.5 - 0.0$ Å *air* wavelength. The calibration performed in THEMIS showed that the angle needed for achieving maximum transmission at 5250.2 Å was 2.1°. A double cavity design was selected in order to have a rapid fall-off in the transmission wings of the pre-filter so that the nearby etalon orders would be reduced below 1%. While this was achieved in the red wing side, the blue side of the pre-filter showed an extended wing that left the secondary etalon peak there at a value slightly above 1%. The spectral calibration of IMaX (Section 8.4) has used this pre-filter curve for its characterization.

Figure 2 IMaX spectral point spread function. It includes an Airy function (three-peaked curve) for the etalon (in double pass) computed from empirical data provided by the manufacturer and multiplied by the Barr pre-filter bandpass curve measured at THEMIS (bell-shaped curve on top).
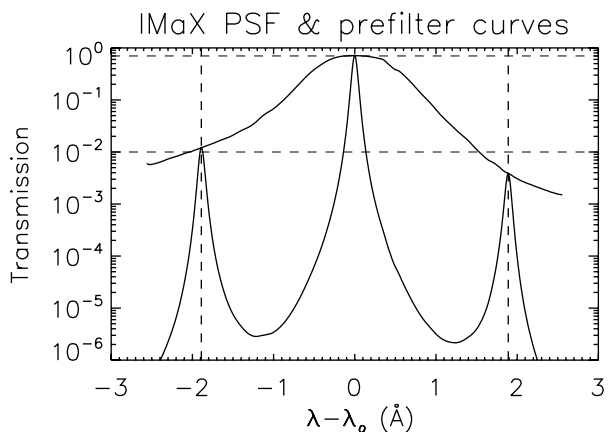
Table 2 IMaX Barr pre-filter characteristics.

Property	Value
Central lambda	5251.15 Å
FWHM	1.05 Å
Working T	35°C
Peak transmission	0.65
Effective refractive index	1.92
Transmitted wavefront	$\lambda/4$
Clear aperture	20 mm
Temperature coefficient	$+0.025$ Å °C^{-1}
Angle for 5250.2	2.1°
Design	Double cavity
Construction	Hard coatings

During the flight, the heater power for the opto-mechanical mounting proved insufficient, and the nominal 35°C was actually never reached. The achieved temperature level was 30 ± 1°C instead. Given the temperature coefficient of the pre-filter, this different temperature meant a bandpass drift to the blue of a mere 0.1 Å, which has a negligible effect.

3.2. The Liquid Crystal Variable Retarder Polarimeter

Two conceptually identical LCVRs were used as the polarization modulator in IMaX. The LCVRs were produced by Visual Display, S.A. (Valladolid, Spain) in a collaboration to produce space-qualified LCVRs (in the context of the *Solar Orbiter* ESA mission, see Heredero *et al.*, 2007). IMaX's LCVRs (see Table 3) use voltages in the range of 0 – 10 V to produce retardances between 535° (at 0 V) and 20° at high voltages. The voltages used for the vector modulation case were [2.54, 2.54, 3.12, 3.12] V for the first LCVR and [2.46, 9.00, 4.30, 2.90] V for the second one. Each combination of voltages for the two LCVRs produces each one of the modulation states, I_i, $i = 1, 2, 3, 4$. The calibration of voltages is explained in Section 8.3. They were selected to reproduce the canonical vector modulation case explained in Martínez Pillet *et al.* (2004). The longitudinal case used [2.292, 2.292] V for the first LCVR, which corresponds to 360° retardance, and [5.293, 2.635] V for the second one, which provides the $\pm \lambda/4$ retardances. It is also important to note that long transitions from high voltages to small voltages are avoided, as they are always slower than transitions from low voltages to high ones. All transitions used here showed response times below 40 ms.

LCVRs are temperature sensitive. For IMaX, a nominal temperature of 35°C controlled to within ± 0.5°C was specified. Since LCVRs share the mounting and temperature control with the pre-filter, their nominal temperature was never reached and the whole system flew 5°C cooler. However, extensive laboratory calibrations performed with the IMaX LCVRs allowed us to determine their temperature sensitivity. The results from Heredero *et al.* (2007) were used to quantify the temperature sensitivity as

$$\frac{\Delta\delta}{\Delta T} = -1.16 + 0.305V - 0.02V^2 \quad \text{for } V < 8, \tag{7}$$

showing a tendency to produce smaller retardances at higher temperatures. δ is the LCVR retardance in degrees, T is the temperature in degrees Celsius, and V the applied voltage in V.

Table 3 IMaX LCVRs characteristics.

Property	Value
Maximum retardance	780 nm
Response time	< 40 ms
Working T	35°C
Peak transmission	0.98
Transmitted wavefront	$\lambda/10$
Clear aperture	25 mm
Temperature coefficient	-1.16 deg °C^{-1}

Figure 3 The temperature-controlled side of the IMaX optical bench including the pre-filter and LCVR mounting (right), the collimator and camera lenses mounting, and the etalon TCPE (left). The stray-light baffle is seen in between the two first elements.
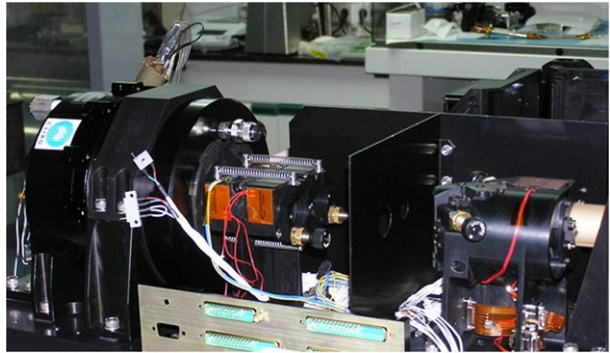
At voltages higher than 8 V, the sensitivity to temperature is negligible for these particular LCVRs.

3.3. LiNbO$_3$ Etalon

Solid LiNbO$_3$ etalons have many advantages for use in autonomous platforms (low weight and parallelism stability among others). However, the most important disadvantage for their implementation in a balloon platform is the use of high voltages for their tuning with the consequent possibility of producing an electrical discharge in the system. The flight pressure conditions were near 3 mbar, exactly the region where air ionization occurs most easily (for both space or ground conditions this is a less severe problem). We thus identify the possibility of an electrical discharge in the kV LiNbO$_3$ system as one of the design drivers for the instrument. The implications were that both the etalon and the HVPS had to be in pressurized chambers located in the optical bench. The connectors between the HVPS and the etalon also deserved special care and avoided the use of outer metallic components.

The LiNbO$_3$ etalons were ordered early in the project because of their relatively long manufacturing time (roughly one year). ACPO/CSIRO built two etalons inside thermally controlled pressurized enclosures (TCPEs) containing a dry nitrogen atmosphere inside, at 1.2 bar. The TCPE internal atmosphere was controlled to within ± 0.03°C and was specified to work at 35°C. This sub-system power was sufficiently dimensioned to reach this temperature with enough margins all along the flight time. The TCPE was ordered with high-quality-grade fused silica windows of 14 mm thickness and 70 mm diameter. The predicted deformation of the windows once the TCPE was in near vacuum conditions was of 380 nm peak to valley over the full aperture. The windows were anti-reflection coated to have almost perfect transmission at 525 and 633 nm.

Table 4 IMaX LiNbO$_3$ etalon properties (25 mm aperture).

Property	Value
Construction	z-cut
Aperture	60 mm
Refractive index	2.3268
Thickness	281 μm
F$_r$ (R)	27.5 (0.892)
F$_f$ (Δ_{rms})	35.8 (1 nm)
F	21
$\delta\lambda$ (single pass)	93 mÅ
Tuning constant	0.335 ± 0.002 mÅ V^{-1}
Tuning speed	1500 V s^{-1}
Working T	35°C
Temperature sensitivity	25.2 mÅ °C^{-1}
Temperature stability	0.03°C
Transmitted wavefront (single pass and windows, full aperture)	$\lambda/23$
Homogeneity (rms fluctuations of peak λ)	16 mÅ

The two etalons acquired from ACPO/CSIRO are referred to as TCE-116 and TCE-117. The best of them in terms of surface polishing is the TCE-116 etalon, but its TCPE developed some leakages through the high voltage connectors and could not be repaired in time for the flight. The TCE-117 was finally installed and was the one that flew in IMaX. Its properties are given in Table 4 (the most substantial difference between TCE-117 and TCE-116 is that the latter had a full aperture wavefront error in single pass of only $\lambda/38$). The properties given in that table refer, unless otherwise stated, to any sub-aperture of 25 mm instead of the full aperture. The IMaX pupil image near the two etalon passes is of this size, or slightly smaller, so the requirements to ACPO/CSIRO were given over any 25 mm sub-aperture. The combination of the IMaX pre-filter and the etalon transmission curve in double pass (the instrument spectral profile) is shown in Figure 2. The pre-filter wings decrease the secondary maximum from the side orders of the etalon to levels of around $1-2\%$. The final spectral resolution achieved by the instrument and the spectral calibration are explained in Section 8.4.

The TCPE cages include a tilt motor to change the incidence angle of the etalon. While this motor was very useful during the AIV phase, the etalon was run at near normal incidence during the whole flight.

Perhaps the largest inconvenience of the LiNbO$_3$ technology for solar observations is the tuning speed. ACPO/CSIRO recommends to use tuning speeds smaller than 1500 V s^{-1} or 0.5 Å s^{-1} (because of the piezo-electric effect of this crystal could damage the wafer at higher tuning rates). As the typical steps used in IMaX for spectral tuning are of about 40 mÅ, the etalon spends 80 ms tuning the wavelength. For jumps of 0.4 Å, that is, the jump corresponding to switching between the continuum point and the first point inside the line, it takes almost a second. This time is relatively long if we compare it with piezo-stabilized systems that use 10 ms or so for virtually all tuning steps. We tested a raw LiNbO$_3$, not polished to etalon standards, for tuning speeds of 3000 V s^{-1} during 15 days satisfactorily (no wafer breakdown or degradation). However, and in order to reduce risks, the tuning speeds during this first flight were kept at the recommended rate of 1500 V s^{-1}.

Table 5 IMaX focal plane detectors.

Property	Value
Chip	FTT1010M
Format	Frame transfer
Max. frame rate	30 fps
Data format	12 bit (4092)
Pixels	1024×1024
Pixel size	12 μm
Full well	170000 e$^-$
QE	25%
Readout noise	50 e$^-$
Dark current	400 e$^-$ s^{-1} pixel^{-1}
Gain	50 e$^-$ DN^{-1}
DC offset	50 DN
Frame transfer time	4 ms

3.4. Focal Plane Detectors

While the original plan was to fly two custom-made, high quantum efficiency detectors, these plans were abandoned, as the requirements for a vacuum-capable detector similar to those that are state of the art in ground instruments were too stringent. Instead, a thermally robust, vacuum-compatible, front-side-illuminated detector was finally selected for IMaX. Two DALSA Pantera 1M30 cameras with 1 k $\times$ 1 k chips (see Table 5) were finally integrated. A frame transfer design with a transfer time of 4 ms allowed us to avoid the use of any shutter mechanism that would have complicated the instrument. The chip itself is protected by a 1 mm thick window in front of it. The camera was mainly selected for its thermal robustness. The chip runs hot (at 45°C) and uses no active cooling mechanism. Thermal control is based on conduction to the front surface of the housing, where it is dissipated. The cameras have no special enclosure for vacuum conditions and have consequently been extensively tested before the flight. One DALSA camera was put in a vacuum cryostat for 18 days working at 4 frames s^{-1} (fps). Thermal conduction was performed using an interfiller and a heat stripe connected to the cryostat housing. The cryostat was cooled by a Peltier mechanism (replaced by a radiator during the flight). The camera survived without any performance degradation, and it was decided to use it in IMaX. The small quantum efficiency ($Q = 25\%$) was considered acceptable only because of the confirmation we had by then (after preliminary design review) of the high transmission of the Barr pre-filter (see Table 2). However, clearly a higher QE camera would have allowed us to obtain more points within the spectral line in the same interval of time (something that would have also required the corresponding communication buses to cope with the higher frame rates).

4. Optical and Opto-Mechanical Design

The IMaX optical power system is all refractive; the mirrors of the system are used only for folding and packaging (see Figure 4). Three mirrors in total are needed. The optical interface with *Sunrise* is the ISLiD focal plane F4 (see Gandorfer *et al.*, 2010). At F4, a field stop confines the IMaX FOV and prevents unwanted light from entering the instrument and
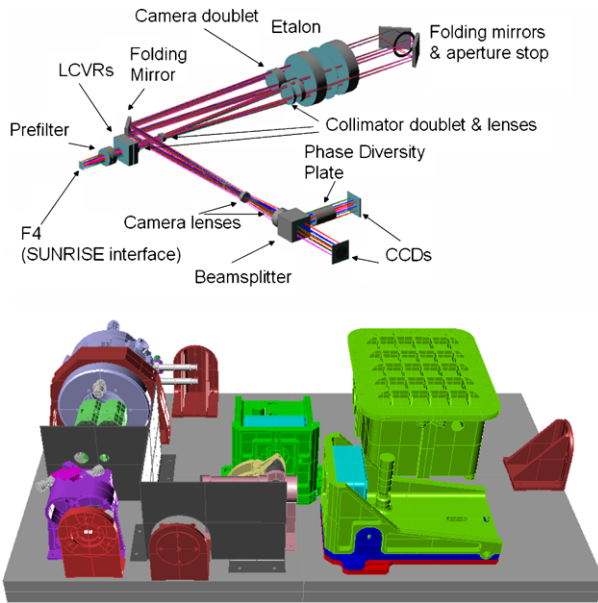
Figure 4 IMaX optical (top; self-explained) and opto-mechanical (bottom) design. In the latter, the F4 plane can be distinguished in a brown-reddish color at the lower left corner. Just after it, the pre-filter and LCVRs housing can be seen in purple. After the stray-light baffle (dark grey), the etalon housing is in blue, preceded by the collimator and camera lenses housing in green. The double light path can be discerned through the two holes in the baffle. To the right-hand side of the etalon enclosure, the vacuum HVPS connectors can be seen in white. After the central baffle, the beamsplitter housing (in pink) appears. Behind it, in yellow, is the PD mechanism. In green are the mountings for the two cameras (bluish) and the PEE. Three isostatic mountings (in brown) for integration into the instrument platform complete the design.

generating parasitic light. This field stop admits two focus positions corresponding to the air and vacuum focus positions, which differ by 1.64 mm in IMaX (the latter being displaced towards the instrument). This shift between the air and vacuum conditions was both predicted by the optical design and checked during the vacuum tests (see Section 8.2). Next, the pre-filter and LCVRs mounting follow at a distance from F4 of about 30 mm (where the focal depth is ±0.66 mm; near the CCDs it becomes ±2.1 mm). After polarization modulation the beam goes through a collimator system consisting of a doublet and two lenses. The focal length of this collimator is 567.36 mm and its F-number is 25, matching the *Sunrise* Telescope and ISLiD F-number. The etalon works in a collimated space producing a blueshift over the FOV. The collimated setup for the etalon requires special care with the maximum angle of incidence on it. The focal length of the collimator guarantees that the angle of incidence on the etalon does not exceed 0.44°, which produces a wavelength drift of 28 mÅ (over the largest circular FOV). The diameter of the resulting collimated beam is 25.6 mm, representing the actual area of the etalon used in each pass. In the collimated space between the two folding mirrors, we locate an aperture stop to adequately set the entrance and exit pupils of the system. The beam is finally focused onto the CCDs by a camera consisting of a doublet and two lenses, with a camera focal length of 1021 mm producing a final image IMaX F-number of 44.99. The image focal plane of IMaX has been designed to be telecentric and so has the object focal plane at F4. Both sub-systems, the collimator and the camera optics, are telephoto lenses in order to shorten the total length of the system and get reduction ratios of 0.53 and 0.57, respectively. The magnification of IMaX is 1.799

in order to get a final image scale of 0.055 arcsec pixel^{-1}. The polarizing beamsplitter is commercial and made of NBK7-Schott glass with anti-reflection coatings on all surfaces. In order to perform phase diversity correction on the image, a parallel plate can be inserted in one of the channels in order to defocus the image on this channel (camera 1). This plate is made of fused silica with 27 mm thickness that produces the specified amount of defocusing corresponding to a phase shift of 1 λ at the edge of the pupil. There are no mechanisms inside the instrument for maintaining IMaX in focus during the flight. For this reason, the most common glass used in IMaX is fused silica, which has near zero thermal expansion (and low stress birefringence). To test and verify the optics of IMaX with a Zygo interferometer (at 632.8 nm), the system has been designed for a wavelength range that includes that of the He-Ne laser. IMaX has thus been achromatized for the range 524.9 nm to 632.8 nm. The materials choice has a great impact on both the achromatization and the athermalization of the instrument. Thus, for the IMaX doublets a pair of glass materials that compensate both the chromatic aberration and the sensitivity to changes in temperature was selected.

The influence on the PSF of retroreflection on optical surfaces (ghost images) was analysed in detail. IMaX includes a high variety of optical components and properties which calls for performing a thorough study on the influence of each surface on the final performances of the instrument. Some of the optical elements, like the etalon and the pre-filter, were considered in a simplified way to reduce the time needed for the stray-light simulation, while still maintaining the strength of the signal. Since the coherence length of light going out from the etalon is quite significant (54 mm for a 50 mÅ spectral resolution), ghost beams should be added in amplitude and not only in intensity. The flux obtained in the detector integrated for the total PSF (including ghost images) has been compared with that obtained from the ghost image alone. The main conclusion of our ghost-image studies was the necessity to tilt the etalon TCPE by an angle of 0.36° around the horizontal axis perpendicular to the light path in order to get rid of the ghost images produced by its windows.

The IMaX opto-mechanical system consists of an optical bench where all the mechanical and optical components are distributed (see Figure 4). To facilitate mechanical manufacturing, all the sub-systems are independent modules. Thus, the instrument contains a mounting for each of these sub-systems:

1. F4 diaphragm
2. Pre-filter and LCVRs
3. Collimation and camera lenses
4. Etalon TCPE
5. Folding mirrors
6. Beamsplitter
7. PD mechanism
8. CCD cameras
9. Stray-light baffle.

The F4 diaphragm has two possible orientations at 180° from each other. In one of the orientations, the field diaphragm is in the air focus position as seen from the CCDs, whereas the other orientation corresponds to the vacuum (flight) focus position. The drawback in the individual mountings policy is that one needs to align each of these mountings carefully. The optical axis was defined as the normal to F4 passing through its centre. The integration process consisted of the individual assembly and verification of each module by sequential order, from F4 to the CCD cameras. This was done with the help of a control metrology machine ensuring a mechanical positioning accuracy better than 25 μm. A higher alignment accuracy was achieved with the help of a theodolite (up to 2 arcsec). Once all the mechanical elements and mirrors were assembled, the power optics (lenses) were mounted.

A stray-light baffle was included in the instrument concept in order to reduce the view factor of the cameras with respect to the zones with maximum scattering power. The baffle can be seen in Figures 3 and 4. All the design calculations have been made with the ASAP code.

5. Instrument Electronics

The IMaX electronics are made up of three main blocks: the main electronics (ME), the optical bench electronics, and the harness. The optical bench contains a proximity electronics (PE), the CCD cameras, and the mechanical, thermal, and optical actuators. Everything is manufactured with commercial-grade, either off-the-shelf (COTS) or specifically designed, components. Both the ME and the PE are enclosed in pressurized vessels (MEE and PEE, respectively) that provide ground pressure conditions during the flight. The harness envelopes are chosen to minimize the outgassing impact in the quasi-vacuum flight conditions. This section is devoted to explaining the various functionalities and the overall design considerations of these three blocks, which are physically and functionally distinct. A block diagram of the IMaX electronics is shown in Figure 5.

5.1. Main Electronics

The ME (see bottom panel of Figure 1) are responsible for the overall control and data processing of the instrument and of the interface communications with *Sunrise*. Their enclosure is physically located on a rack along with the other instrument electronic boxes and the platform control electronics.

The main functionalities of the IMaX ME are ensured through five sub-systems: the CPU board, the real-time image processing board (IPB), the interface (I/F) board, the etalon thermal control, and the power supply (DC/DC board).
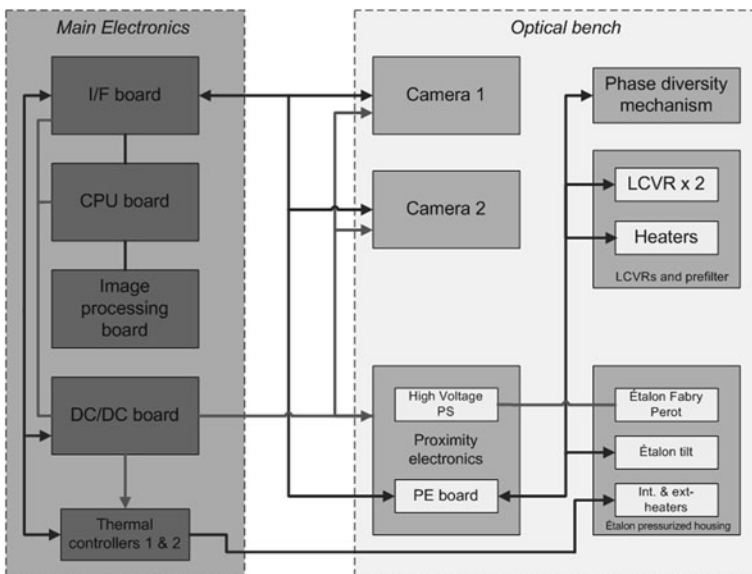
Figure 5 IMaX electronics block diagram.

The CPU board is a COTS VL-EBX-12b board from Versalogic Corporation that uses a PC/104 expansion bus and an SDCFX3-4096 solid state, massive storage, 4 GB disk from SanDisk that includes the operating system and all the specifically designed software (see Section 5.3). It has the following features:

- Pentium 3 Mobile microprocessor @ 1.6 GHz
- 512 MB RAM
- 4 GB, compact flash memory disk
- Two Ethernet 10/100 ports
- One PC/104-Plus slot used by the SMT374-300 board
- Two COM ports (RS-232) and two COM ports (RS-422)
- Eight-channel, analog-to-digital converter with 12-bit resolution
- 32 channel digital input/output
- Graphic video
- Watch-dog timer.

This board is in charge of

- booting the system from an NVRAM memory and from the disk,
- initializing the different sub-systems,
- controlling the different sub-systems,
- carrying out watch-dog tasks,
- communicating with the PE and the IMaX optical bench,
- switching on and off the secondary power supplies,
- compressing images to be stored,
- and communicating with the *Sunrise* Instrument Control Unit (ICU).

The IPB is implemented through a mezzanine board with an SMT-310Q PC104 carrier and a Sundance SMT374-300 board. The latter includes two Texas Instruments C6713 DSPs (digital signal processors) and one Virtex-2 XC2V2000 FPGA (field programmable gate array) from Xilinx. The board runs at 200 MHz and has two SDRAM banks of 128 MB each. DSP 1 is in charge of the communications with the embedded CPU and the PE. It also has demodulation and truncation capabilities of the accumulated images. DSP 2 performs image accumulation according to the different observing modes and sub-system (etalon, LCVRs, CCDs, PD mechanism) synchronization. The communications between this board and the CPU, the PE, and the CCDs are carried out through the FPGA.

The interface board has been introduced for mainly historical reasons. As commented on earlier, the first customized cameras chosen for IMaX had to be changed in a quite advanced step of the design due to a failure of the supplier in providing them such that they complied with the specified requirements. To keep the on-line processing developments as unchanged as possible, the easiest solution at that point was to introduce this board that simulates the foreseen behavior of the former cameras with the COTS ones. Therefore, all the communications with the cameras are indeed made through this board, which also controls the housekeeping signals conditioning of the ME box.

The functionalities of the remaining two sub-systems are fairly clear. The etalon thermal controller maintains the interferometer within the specified range of temperatures. It is implemented with one PID 2216e controller from Eurotherm that provides an accuracy of $\pm 0.03°$C. A second PID device controls the ambient surrounding the TCPE to within $\pm 0.5°$C. The specifically designed power supply feeds the different sub-systems and the MEE fan. The supply is made from a DC non-regulated voltage provided by the platform, taking care of the necessary efficiencies to prevent power losses, allowing soft starts for

in-rush current minimization and sequential switch-on of the sub-systems, and containing the necessary filters to maintain electromagnetic compatibility with the other instruments aboard *Sunrise*. All these features follow a strict grounding and bonding scheme (similar to that in space applications), hence avoiding current returns.

5.2. Optical Bench Electronics

Due to the long cabling distances between the MEE and the OBE, the proximity electronics (PE) have been placed in a pressurized enclosure near the optical components mainly because of the presence of the HVPS. We took advantage of the PEE to install additional electronics in order to avoid voltage drops and noise generation and to reduce the number of wires, reading errors, *etc*. The main functions of the PE are:

- LCVR signal generation and thermal control,
- etalon tilt motor and high voltage power supply control,
- synchronization between changes of the etalon wavelength sample and the LCVR retardation angle,
- acquisition of the optical bench housekeeping parameters,
- provision of power drive for the heaters,
- generation of the different voltages for the sub-systems,
- reset and clock generation,
- and communications with the ME.

All these functions are carried out by a specifically designed board using a non-volatile 1280 AX FPGA from ACTEL as a main controller for peripheral devices such as the HVPS or the controllers for the LCVRs and the PD mechanism.
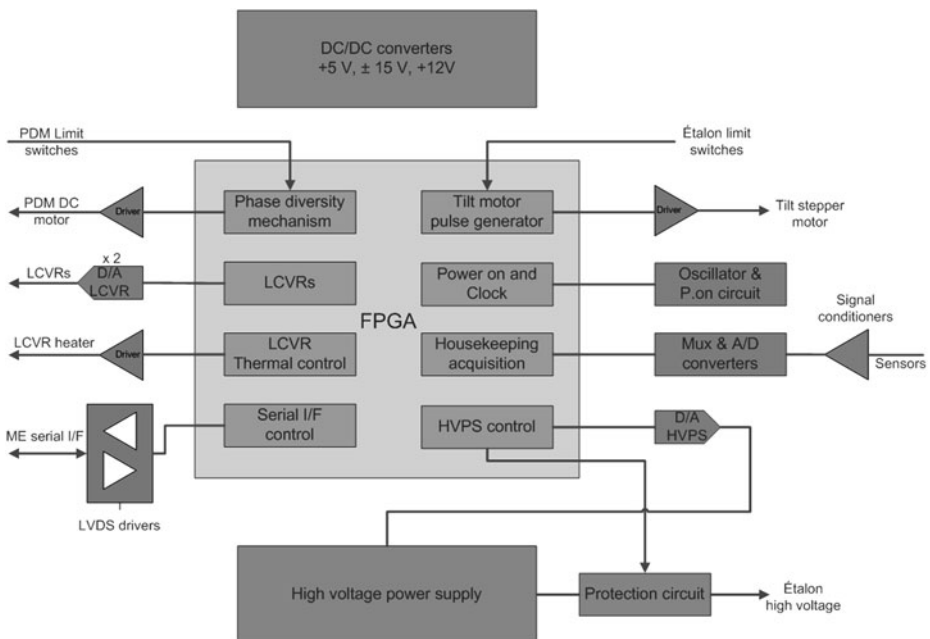
Figure 6 IMaX proximity electronics block diagram.

A block diagram of the PE is shown in Figure 6. The DC/DC converters are included in order to avoid several different voltages travelling between the ME and the PE through a long harness. High efficiency DC/DC converters have been selected, hence minimizing power losses. The low-voltage differential signalling (LVDS) driver block is formed by transmitter/receiver pairs compatible with the LVDS electrical standard. The communications with the ME are carried out by the FPGA through a customized, serial-synchronous interface with five lines from the ME and two lines to the ME. The block labelled MUX and A/D includes an analog multiplexer and a 12-bit resolution analogue-to-digital (A/D) converter with a range between 0 V to $+10$ V. It constitutes a 16-channel acquisition system for temperatures, pressures, and voltages. The signal conditioners are in charge of adapting the different analogue voltages to the range of the A/D converter. The LCVRs D/A converter module has two devices to generate the analogue signals needed to control the retardance in both liquid crystals. A 1 kHz, square wave voltage-modulated signal is generated between the FPGA and this module with an amplitude of ± 15 V. Applied to the LCVR, this signal produces a retardance controlled by the amplitude of the applied voltage. This signal should later be adapted in impedance by an LCVR analogue driver. A similar D/A converter is in charge of controlling the HVPS. A COTS, HP5RZC bipolar power supply between ± 5000 V from Applied Kilovolts, Ltd. has been used. The output of this HVPS is linear to the input. After calibration, $V_{\mathrm{out}} = 448.22 V_{\mathrm{in}} + 13.14$ with all quantities in volts. The input range goes from -10 V to $+10$ V. The converter resolution is 16 bit, thus providing the required accuracy for voltage control. To prevent any damage in case of power supply failure, a circuit using a high voltage relay has been included that allows a slow discharge of the etalon when the supply is off.

The cameras (see Section 3.4) are able to reach up to 30 fps with a 12-bit resolution. The nominal speed during flight was 4 fps. A serial interface based on channel link is used allowing one to employ just four fast lines for transmission and one line for triggering plus two slow lines for serial control. Two operating modes (out of the possible six) are used, namely the external frame rate and exposure time mode for integration times greater than 1 s (only used for assembly, integration, and verification procedures), and the external frame rate and internal exposure time mode for integration times less than 1 s. Synchronism between the two cameras is allowed within both operating modes. Commands are sent to the cameras by following a serial, asynchronous interface standard with hardware handshake.

Two motors are installed inside IMaX, but they are not used under normal observational conditions. They are only used for calibrations, either during flight or for the various ground-based check-outs. The phase diversity (PD) mechanism is actuated by a Maxon DC motor operated at 12 V. Two position limit sensors report on the state of the bi-stable device. This motor was extensively used during the flight. The proprietary linear actuator inside the TCPE, which controls the tilt angle of the etalon, is based on a stepper motor driven by the PE, and it was provided by ACPO/CSIRO. This capability was used during the assembly, integration, and verification phase of the development, but not during the flight, when the etalon was always at normal incidence.

5.2.1. Harness and Connectors

Data and signal links between the electronic boxes use differential techniques with twisted pair wires for best common-mode noise rejection and ground loop prevention. The harness is protected against electro-static discharge effects and radiated electromagnetic emission and susceptibility by overall shields. These shields provide full coverage of all internal wires and inner shields. The coverage includes stress relief areas at the connector backshells. The

overall shields are electrically connected to the structure ground level. To provide well-defined low impedance ground connections, overall shields are attached to connector pins on both harness ends. The dedicated connector pins of the unit or box receptacle are connected to the structure ground via short (< 5 cm) straps, in order to avoid loop-antenna-induced high frequency noise. The harness and connectors outside the pressurized boxes are vacuum compatible. The harness insulators are made of polytetrafluoroethylene derivates. Polyvinyl chloride is avoided for outgassing reasons. Connector crimp contacts are used. Soldered contacts are avoided because of the difficulty in cleaning flux-contaminated wires. Cables, especially those inside optics compartments and on the telescope, are cleaned and baked out before processing or harness manufacturing. All external connectors to the ME are space-qualified D-sub connectors plugged to vacuum feed-throughs installed in the enclosure walls. Vacuum circular connectors from LEMO have been used for the PE.

5.3. Instrument Software

The IMaX flight software is divided into two main blocks: the control software (CSW) and the image processing (or DSP) software (DSW). The CSW is mainly devoted to image compressing and formatting, telecommand and telemetry management, and sub-system control. The DSW mainly deals with image acquisition, (on-demand) demodulation and truncation, hardware (HW) control, and interfaces with the CSW. Thorough validation procedures, similar to those required by the European Space Agency for space missions, were applied to the system after every change in any piece of software during the assembly, integration, and verification phase.

5.3.1. Control Software

A functional diagram of the CSW is shown in Figure 7. The system on/off module controls the start up and shut down processes of IMaX. The system update module implements software upload capabilities if required during the flight. The module labeled UDP manages the acceptance, validation, and execution of user-defined commands and programs (see below). The scheduler handles the (periodic or single) event tasks like housekeeping parameter (HK) generation and contingency detection. A specific module is devoted to detecting contingencies and running the appropriate recovery actions. The logger module is in charge of writing a set of files with all the relevant system actions and events. Another module changes the various operative modes (see below). Finally, the three I/F boxes in the diagram correspond to ICU, hardware, and DSW interfaces. Telecommands (TC) and telemetries (TM) are sent and received through the first of these interfaces; internal commands and data travel through the other two. In addition, time synchronizations and log parameters stream through the DSW I/F. Windows XP was finally selected as the most suitable operating system for all the IMaX purposes mostly because of the requirements of software development for the SMT374-300 board. All the non-critical services of the operating system are disabled, and those files that are not used are removed in order to minimize the start up time.

Three main concepts are involved in the IMaX software development: the context file (CF), the defined commands (DECOs) and user-defined programs (UDPs), and the operative modes. A CF is an archive containing all the input system variables, *e.g.*, the default observing mode and its consequent values for wavelength samples and LCVR voltages, the maximum and minimum allowable values for temperatures in order to trigger contingency actions, *etc*. There is always a default CF stored in the CPU board storage disk which is used provided no other CF has been sent from the ICU (automatic time-line operation) or

Figure 7 IMaX control software functional diagram.
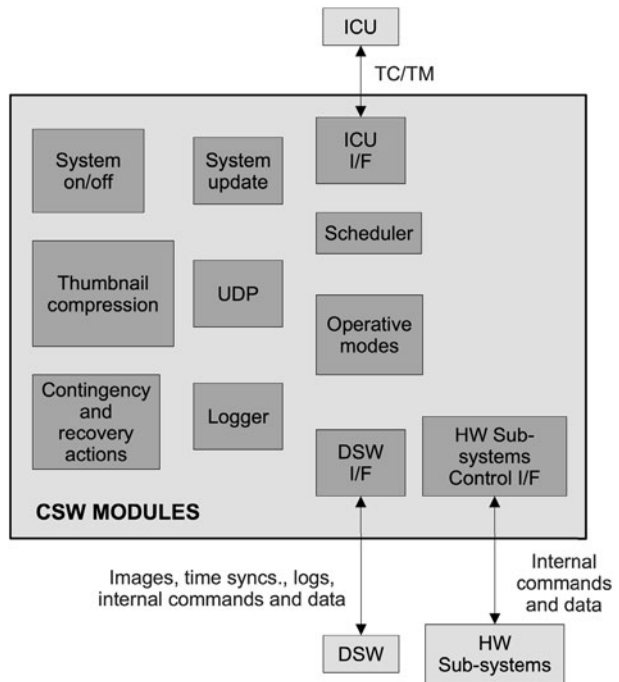
the ground support equipment (remote operation). All the variables in the operating CF can be modified either individually or in unison through appropriate TCs. A set of specifically designed commands (DECOs) constitute the basics of the CSW and represent all the necessary elementary actions needed to operate the instrument and debug the CSW itself. They can be grouped as follows.

- General DECOs: Used for the CSW syntax (*e.g.*, loop creation), for calling UDPs (see below), write comments, *etc*.
- System DECOs: Aimed at controlling the system (*e.g.*, start up, shut down, reset, *etc*.).
- Sub-system DECOs: Control the various functionalities of the sub-systems like the cameras, the PE, and the thermal controllers.
- Operating and observing mode DECOs: Provide the configuration values for each mode.
- HK DECOs: Ask for the various HK parameters.
- CF DECOs: In charge of modifying or verifying the CF.
- Debugging DECOs: Needed to build meaningful UDPs.

A UDP is just a collection of DECOs and represents a given high-level action like constructing a piece of the observation time line. There are three operative modes for the CSW: the safe, change, and science modes. The system is in safe mode just after start up, just before shut down, or upon request by the user. In this mode, the OB electronics are off and UDPs can be run. In science mode, the instrument performs all the automatic activities corresponding to the current scientific observing mode. No UDPs can be run in this mode. Any change between these two operative modes is preceded by putting the system in the change mode. When in this mode, manual operations like those during the AIV phase can be carried out because UDP running is allowed.

**Figure 8** IMaX DSP software block diagram.
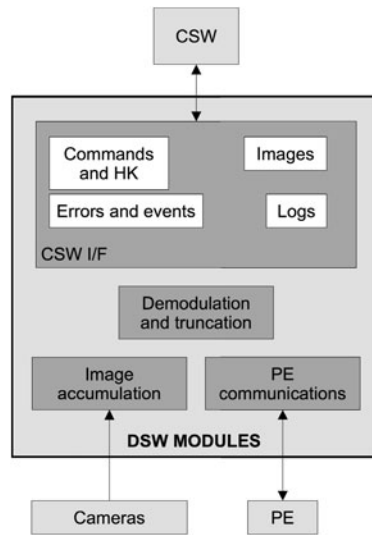
5.3.2. *Image Processing Software*

The main functions of the DSW are sketched in Figure 8. Among the communications with the CSW one can find the reception of and response to general commands and those concerning the HK, the sending of pre-processed images; information on errors and other special events, and the sending of logs. The DSW is also in charge of image acquisition and accumulation in the different observing modes. These processes are carried out in real time, so that the accumulation and exposure times are equal. Periodic triggering of the cameras is made with an accuracy of ± 1 ms and with a period equal to the exposure time plus 4 ms (camera internal transfer plus erase times). All the accumulations are made with 16-bit words. The communications with the PE consist of the transfer of values corresponding to the etalon and LCVR voltages, and the state parameter of the PD mechanism. Likewise, the accuracy in the camera synchronism with LCVRs is better than 1 ms. The demodulation coefficients are received from the CSW and then applied (if necessary) to the polarized images, making the intermediate calculations in signed 32-bit words in 2's complement. After demodulation, images are truncated (bit-shifted) by 15 bits plus those specified (3) for the different observing modes. As discussed earlier, no need for on-board demodulation was present during the first flight.

5.4. Data Flow

In summary (see Figure 9), once the observing mode (see Section 4) is selected, the CSW sends the configuration parameters to the DSW. The latter sends the corresponding commands to the cameras (exposure time and mode) and to the PE (LCVR and etalon voltages plus the state of the PD mechanism). Images are acquired and then sent to the I/F board, which stores one of them per camera. The two images are then sent to the image processing board (IPB) to be accumulated and buffered (according to the current observing mode). After a complete set of images is obtained, they are demodulated and truncated (if needed) and sent to the CSW, which is in charge of compressing (JPEG-LS) and formatting them. They are finally sent to the ICU for storage. Truncation is made by 3-bit shifting, hence removing

Figure 9 IMaX data flow.
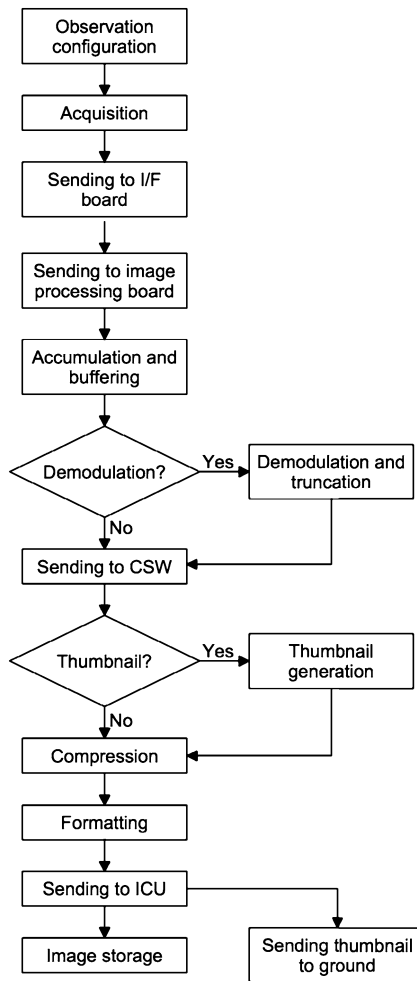
the three less significant bits that are enough to preserve a S/N of 10^3. The *Sunrise* telemetry bandwidth is not wide enough to send all the images to ground. The on-line monitoring needs make it necessary to specifically process a sub-set of the images for them to have a smaller size. These particular images are called thumbnails and are constructed by either binning or cropping the original ones (which are nevertheless preserved) by a programmable factor. Thumbnails are sent to the ground station by TMs.

6. Thermal Design

The IMaX thermal design was conceptually envisaged to be as simple as possible while also capable of providing temperatures within the working range for the various sub-systems. First of all, and in order to obtain an effective thermal control, the IMaX OBE was conductively and radiatively isolated from the environment. It uses a radiator as a top cover to reject the excess heat from the dissipative elements. Second, a sensible arrangement of the elements on the optical bench was performed together with a careful thermo-mechanical

design including the selection of proper coatings and materials. The OBE is attached to the Post-Focus Instrumentation platform (PFI) by kinematic mountings at three articulate joints that provide a poor thermal conductance (the three brown isostatic mounts in the bottom panel of Figure 4). In order to maximize radiative isolation from the environment, the lateral sides of the OBE (seen in the bottom image of Figure 1) were finished in Alodine. The bottom side was covered with a polished aluminium foil, and the outer radiator surface was painted in white with Aeroglaze 9929 and Aeroglaze A276 coatings. The interior of the OBE was finished in black with a double purpose: stray-light avoidance and better thermal coupling between the elements.

From a thermal point of view, the OBE is divided into two areas. The area where the pre-filter, the LCVRs, and the etalon are located uses active heating to provide a thermally stable environment. The requirements for each optical sub-system have already been mentioned, but the idea is that this area of IMaX has optical components with temperatures in the range of 25°C to 35°C and with active control implemented to various degrees of accuracy. The LCVRs and pre-filter mountings are heated with an 8 W thermostat, whereas the optical mountings on both sides of the TCPE use a 3.5 W thermostat. The TCPE itself included a 20 W thermostat. The other area of the IMaX OBE contains the CCDs and the PEE with electronic components with temperatures in the range −10°C to 40°C. Most of the power dissipation takes place in this area, and four ammonia heat pipes are used to direct this heat to the radiator on top of the OBE. Two heat pipes are connected to the sides of the PEE and one heat pipe to the front side of each of the CCD cameras.

During the flight, neither the LCVRs and pre-filter, nor the doublets and lenses reached their nominal temperatures (35°C and 30°C, respectively). Instead they worked typically at 31°C and at 27°C with a diurnal fluctuation of ±1°C. It is clear that the power of these heaters was underestimated for an Arctic flight. In part, this was due to the fact that the power consumption of the instruments was considerably smaller than what was originally envisaged, so the instrument power dissipation and mean temperatures were smaller than expected (both in the OBE and in the MEE). The consequences of these lower temperatures had to be considered in the data calibration of the instrument (see Sections 8.3 and 8.4).

The MEE was located on one of the *Sunrise* racks attached to the gondola rear part, so that its surrounding environment was quite different from that of the OBE. The electronic boards were bolted to an aluminium grid-frame fixed to the chassis box's bottom face. A fan was located in the middle of the box in order to provide a homogeneous interior temperature, reducing hot spots with a proper air speed that also helped to increase low temperatures where necessary. Six temperature sensors, type AD590 FM, were glued both on the box chassis and on the key electronics components to monitor their temperatures. MEE temperatures during the flight were found to be on the cold side of the expected range, reaching in some parts temperatures below zero. Nevertheless, the established temperature range for the electronic components, −20°C to 40°C was never exceeded, with the unit working properly at all times.

7. Pressurized Enclosures

Two pressurized vessels have been developed to protect the IMaX electronics (commercial grade electronics) from the mission environmental conditions: the MEE and the PEE (see Figures 10 and 11). The MEE is attached to the *Sunrise* electronic platform and the PEE to the optical bench. Since the optical elements must be extremely stable, the PEE design has particularly addressed the stability of its interface with the optical bench, while the MEE

Figure 10 The pressurized IMaX MEE mounted into the flight panel.

has avoided deformations in its interface with the *Sunrise* electronics platform during the mission. Each enclosure (MEE and PEE) is basically composed of a base, a top cover, and the electronics support frames. The PEE, which contains the HVPS, also includes an internal insulator that separates its interior into two compartments and that provides insulation between the HVPS and the rest of the electronic components to avoid electromagnetic interferences between them. Following thermal design guidelines, the outer MEE surfaces have a layer of thermal paint to optimize heat rejection over the Alodine 1200S treatment, while the outer PEE surfaces have been sulphuric anodized and black dyed like the rest of the IMaX opto-mechanical elements.

The base has an attachment flange to receive the seal gasket and the screws to maintain, together with the top cover, the pressure at any stage of the mission. Spring washers are used to maintain the sealing during flight time and, additionally, all the screws are fixed with epoxy adhesive. Strengtheners that guarantee the stiff behaviour of the structure while maintaining a thin wall (to reduce mass) have been included in both the base and the top cover. Due to environmental temperatures and to external agents, resistance fluorosilicone elastomer has been selected as an O-ring material for the sealing. A problematic area for any sealed compartment is the connectors. For IMaX, we use hermetic connectors for data and power lines. A high voltage connector (specified for up to 20 kV) has been included in the PEE for the HVPS. Each enclosure includes two purging valves. This purging system allows

the ambient air inside the box to be replaced with dry nitrogen once it has been closed and sealed. The enclosures were purged and filled with nitrogen at a pressure of 1.2 atm. No leakages were detected during the entire flight.

8. Instrument Calibration

This section describes the calibration of the three main functionalities of the instrument (imaging, spectroscopy, and polarimetry) in air and in vacuum conditions as well as before and after integration with the ISLiD and the telescope.

One of the major problems encountered during the AIV phase was the reduced light levels with which the instrument was illuminated after inserting the Barr pre-filter. Due to the small bandpass of this pre-filter, light levels were reduced dramatically even when high power lamps were used. Often, the instrument had to use integration times of several seconds, for which it was not originally conceived.

8.1. Image Quality Characterization. Phase Diversity

Image characterization of the instrument at various stages during the integration was done in two independent ways. First, standard interferometric techniques at 633 nm were performed wherever possible. As the laser light could not be used after insertion of the pre-filter, these measurements were complemented with PD analysis to characterize the residual aberrations due to the built-in capability of the instrument. The use of the PD technique has proven to be very useful at all stages of the AIV phase.

After inserting all the elements with optical power, the optical axis of the instrument was found with a 2 arcsec accuracy. The telecentricity of the instrument was checked by projecting an illuminated reticle at infinity (as seen from F4) and visually observing the image of the reticle formed at the pupil plane between the two folding mirrors behind the etalon. The interferometric tests, using a retroreflecting ball system in each of the two focal planes of IMaX, with the full optical setup of IMaX (without the pre-filter and the etalon), showed the instrument optical quality to be $\approx \lambda/15$, well within specifications. Before inserting the

Figure 12 The Zernike coefficients describing the image performance of IMaX. Top: After integration at INTA with a global $\lambda/10.5$ rms WFE. The c6 coefficient corresponds to the astigmatism generated by the etalon. Bottom: Performance inferred during the flight with a global rms WFE $\lambda/5.4$. A defocus component of 0.5 mm (at F4) is obtained.
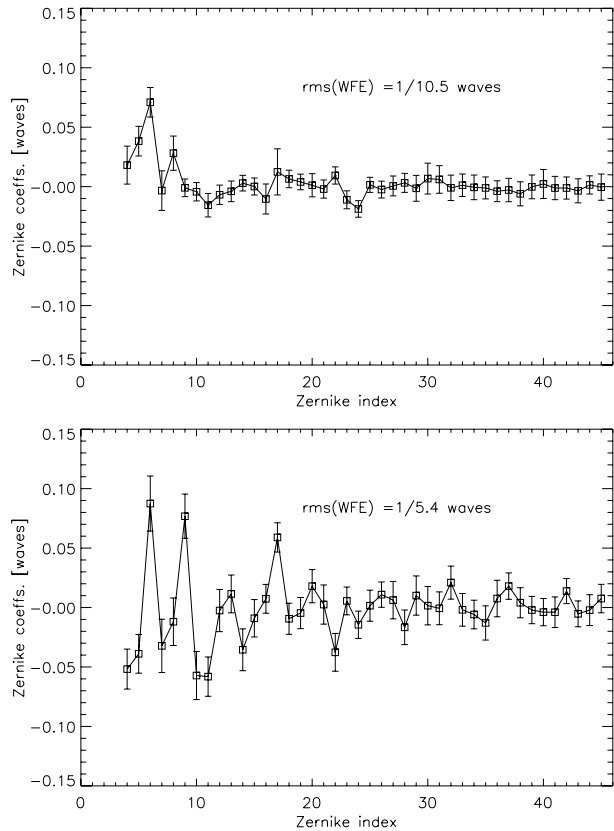
TCE-117 etalon, interferometric measurements were made to characterize its optical quality. In spite of the fact that the manufacturer-measured wavefront errors were as small as $\lambda/23$ (see Table 4), we detected a noticeable astigmatism component that degraded the quality to $\lambda/11$. The reflection of a projected reticle by a theodolite on the etalon surface showed an astigmatic figure that was incompatible with the manufacturer's quotation.[3] After integrating the etalon in the optical path, the combination of the $\lambda/15$ from the optical components and the $\lambda/11$ from the etalon became dominated by the latter. Thus, the figure for the overall rms WFE of IMaX, as delivered for integration in *Sunrise*, was $\lambda/11$ (Strehl ratio of 0.7). This was confirmed by PD inversions made with a bunch of optical fibres located in F4 used as the image object. 24 PD-pairs (at 522 nm, the pre-filter was not yet in) were acquired using the two cameras. Defocusing here was performed by moving the fibre bunch through the focus position by known amounts allowing the inference of the aberrations in both channels. The left panel of Figure 12 shows the Zernike coefficients (from the term four-defocus-onwards in the Noll, 1976 basis), characterizing the aberrations of the system. The rms WFEs, derived from these calibrations (with the etalon set to different voltages), range from $\lambda/9$ to $\lambda/17$ with a mean value of $\lambda/11$. In all cases, the plots of the retrieved Zernike coefficients look very similar. A common feature in all of them is a notable con-

---

[3]We emphasize that the detected astigmatism was a figure error due to a low order aberration. TCE-116 was, on the other hand, measured to be at the manufacturer's value of $\lambda/38$.

tribution of the 6th term (c6, third order astigmatism) that should be ascribed to the etalon. While the TCE-116 would have offered a better image quality performance, the time needed to perfectly seal the TCPE of this etalon was too long to consider its replacement, and it was decided to fly the TCE-117.

Once the pre-filter was inserted, which is close to a focal plane, these calibrations were repeated with similar results, in particular the astigmatism represented by the 6th coefficient, but the data were noisier due to the lower light levels. Additionally, the inclusion of the pre-filter (which made the instrument monochromatic) brought up interference fringes from various components that made the analysis more complicated (see Section 9.1).

The detected astigmatism implies the presence of a sagittal focus and a tangential focus. The distance between these two foci is 1.6 mm (at F4), a number similar to the focus depth. This implies that during integration of the instrument with the ISLiD, an effort was needed to find the best compromise focus where the instrument performance was maximized. This, of course, required aligning the two instruments below 1 mm along the optical axis. To this end, an illumination setup simulating light from the telescope and with an accessible pupil plane was established at MPS laboratories. A Hartmann test, masking the pupil in the horizontal and vertical directions, with IMaX at various focus positions, was made and the best sagittal and tangential foci were established to a fraction of a millimeter. Once at the air focus position, a PD calibration was made to characterize the optical quality of the ISLiD and IMaX combination. Note that in this case all the optics are in place, providing low illumination levels and generating interference fringes. The etalon was tuned to maximum transmission of the pre-filter (voltages close to those used during the flight). Yet the PD characterization made with a Siemens star target at F2 (the ISLiD entrance focus) resulted in a global WFE of $\lambda/15$ (and with a similar c6 coefficient as observed with IMaX alone). This characterization confirmed that we had found the best air focus, as no significant defocus term appeared in the corresponding Zernike coefficient. This basically means that the ISLiD was transparent in terms of optical quality at the IMaX focal plane. Clearly, our portion of the ISLiD has an optical quality well above $\lambda/15$. Once the air focus was found, IMaX was moved to the vacuum position by displacing the instrument towards the ISLiD by 1.64 mm. Another PD characterization was performed at this new position; the result was that the vacuum focus position was achieved, but the noise of the data was large enough not to ensure a better focus position within 1 mm. The instrument was left in that position for its transportation to ESRANGE.

All these calibrations provided a wealth of information that has been very useful in understanding the in-flight performance. The bottom panel in Figure 12 provides a PD calibration performed on the second day of the flight. The overall rms WFE is $\lambda/5.4$, which is smaller than the performance we observed in the air focus of the ISLiD and IMaX combination. This discrepancy has to be understood in terms of the additional effects introduced by the telescope and other in-flight generated aberrations. In particular, the PD calibrations have shown the following effects to dominate.

- The PD check done at MPS on the translation of the air-to-vacuum focus was only able to confirm the vacuum focus position to within ± 0.5 mm. Values near the extreme of this range can significantly degrade a $\lambda/11$ performance. Indeed, from the PD analysis of the flight data shown in Figure 12, we deduced a defocus of a magnitude close to 0.5 mm.
- The intrinsic astigmatism of IMaX (c6) is, of course, present but slightly increased with respect to ground calibrations.
- Trifoil terms (c9, c10) have appeared that we ascribe to the mirror mounting (but we have no real confirmation of this).
- A spherical aberration is detected that was not seen before.

Note that we do not know what part of the defocus and spherical aberration could originate in the lack of stable pointing of *Sunrise* at the level specified as explained in Berkefeld *et al.* (2010). The residual high frequency jitter, estimated from the Correlation Wavefront Sensor (CWS) residual pointing errors, shows high frequencies (>30 Hz) with amplitudes of $0.03 - 0.04$ arcsec (almost one IMaX pixel) whose direct effect will be a blurring of the image similar to a defocus and/or a spherical aberration. As this jitter is associated with high frequencies, one could assume that this is a residual aberration that is constant in time, in much the same way as a real optical defocus of the system.

Despite the degraded performance as compared to IMaX on-ground calibrations, having a WFE above the minimum threshold estimated by previous studies (see Section 2.1) makes us confident that near-diffraction imaging is achievable with IMaX data (see Section 9.1).

8.2. Vacuum Tests

Vacuum tests of IMaX were included in the AIV plan with three interrelated objectives: to test and verify the functionality at simulated (varying) flight thermal and pressure conditions, to test the difference between the best focus position in vacuum and in air, and to test the appearance of arcing in the HVPS-etalon cabling system.

The IMaX optical bench was introduced into a thermal vacuum chamber that includes optical quality flat windows that can be used to feed light into the instrument (see Figure 13). The vacuum chamber has a base plate where the optical bench was mounted and whose temperature can be controlled. The chamber also includes a shroud that surrounds the instrument under test and whose temperature is also controllable. The temperatures of these two elements were cycled between $16 - 24°$C over several hours (to simulate the diurnal variation expected during the flight).

In order to check the image quality in vacuum, including checking the position of the vacuum focus, a slit was placed at F4 and images were taken with the full system (the MEE was outside vacuum). This test was made without the pre-filter in the instrument, as

Figure 13 The IMaX optical unit in the thermal vacuum chamber at INTA facilities for testing the instrument performance under flight conditions. Light can be fed to the instrument through an optical quality, flat window.
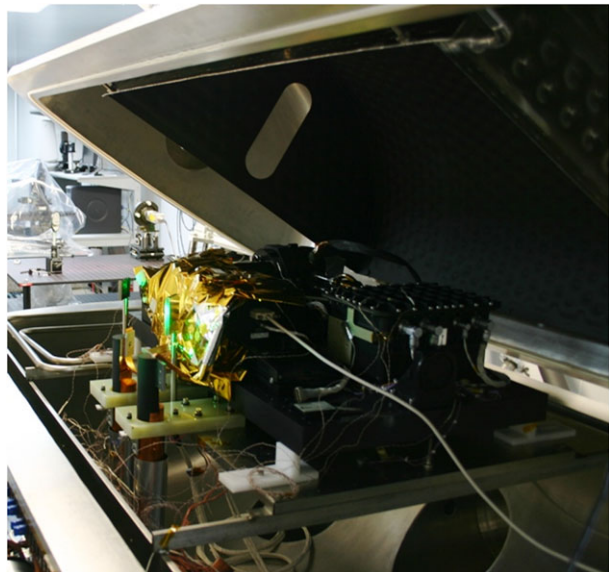
this would have limited enormously the available amounts of photons. Instead a broad-band (100 Å FWHM) pre-filter was used, thus allowing slightly more than 50 orders of the etalon to contribute to the final image. No heat pipes were implemented in the instrument, and heat from the CCDs and PEE was evacuated with thermal straps to the base plate. The functional tests included LCVR modulation, application of etalon voltages, PD mechanism insertion, and image acquisition. All heaters and thermal sensors were already integrated in the instrument and their performance monitored during the test. In this case, all temperatures achieved were nominal, and no shortage of power was evidenced for the LCVRs, pre-filters, and etalon environment heaters. However, the temperatures in the actual flight were cooler than the minimum one used in this test, which prevented them from reaching their expected values. All other instrument functionalities tested in this vacuum test resulted in nominal conditions with the exception of the arcing observed in the connectors of the HVPS. When working at 3 mbar and when the applied voltage was higher than 1 kV (absolute value), arcing was observed between the inner and outer metallic components of the external connectors. To solve this problem, all metallic parts were removed from the external connectors, and a ceramic solution was adopted.

8.3. Polarimetric Calibration

The polarization calibration of IMaX followed a two-step process. First, the two LCVRs of the flight pair were characterized individually and then together in a typical analyser combination before integrating them into IMaX. The best voltage combination to maximize the polarimetric efficiencies was found in this way (for the nominal flight temperature, see Section 3.2). In this calibration, sufficient time was given to the LCVRs to attain the corresponding retardance value, and no voltage optimization including finite switching time effects was performed. The setup used in this calibration consisted of a fixed linear polarizer followed by a quarter-wave plate[4] in a rotating mount and stepped from 0 to 355 degrees every five degrees, thus providing 72 calibration measurements. Before the detector (a photodiode in this case) a fixed linear polarizer was used as analyser (and oriented parallel to the entrance linear polarizer). This setup allows a least-squares determination of the **M** and **D** matrices and their errors. The entrance linear polarizer was vertically oriented, thus fixing the x-axis (positive Q) direction of the modulation matrix. Once the voltages providing near-maximum efficiencies were found, the two LCVRs were put into the corresponding opto-mechanical mount and integrated into IMaX. A characterization of the IMaX polarization modulation properties using the same linear polarizer and rotating wave plate combination was then made. The analyser now was the instrument beamsplitter, and the detectors were the instrument CCDs. This calibration was made before inserting the pre-filter into the system to maximize the light levels; a 100 Å pre-filter was used instead. Under this configuration, two **D** matrices were derived using 1 s and 0.25 s exposure times and compared to investigate the effect of LCVR finite switching times in this exposing range. The differences between the various matrix terms were less than 2%, and no further optimization was considered necessary. The efficiencies achieved under these conditions (broad-band illumination) were $\epsilon_{Q,U,V} = 0.56, 0.57, 0.52$, which are well above the requirements (see Section 2.1).

After the 1 Å FWHM IMaX pre-filter was inserted, the usable light levels in the laboratory dropped dramatically, as now only one etalon order was entering the instrument.

---

[4]Its exact retardance was found by analysing the results of a calibration run with no LCVRs inserted.

Figure 14 Top: IMaX polarimetric calibration with the eigenstate generator from Meadowlark. Bottom: IMaX spectroscopic calibration using an iodine cell at the entrance of the instrument.
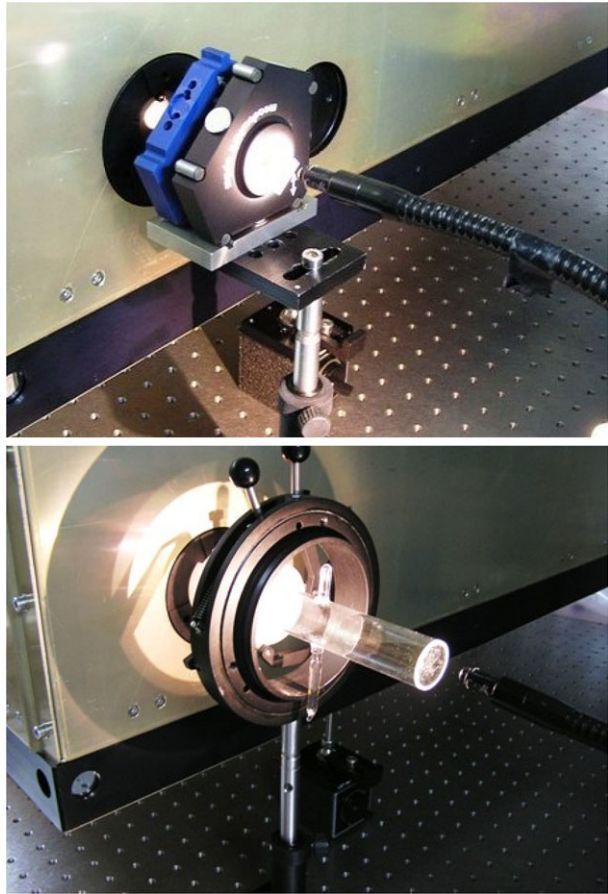
All calibrations were made with laboratory lamps, and this filter required exposure times of 1 s and 20 accumulations at each polarization state in order to achieve decent signal levels. A procedure including 72 measurements as before under these circumstances would have been prohibitively long. Instead, an eigenstate calibration system from Meadowlark Optics was used that generates six polarization states in a highly repeatable way (see Figure 14). This eigenstate generator allowed for orientation accuracies of 1 arcminute and the retardance of the quarter-wave plate was known with an accuracy of a tenth of a degree, ensuring calibration of IMaX demodulation matrices to better than 1%. The nominal linearly polarized states at 0°, 90°, 45°, and 135° together with the right and left circularly polarized states are generated to estimate the **M** and **D** matrices. Note that this time 24 measurements are used to evaluate the 16 matrix coefficients (instead of 288 as before) and no practical inference of the uncertainties can be made. The only way to estimate the precision of the various matrices is by repeating the measurements and observing the changes in their coefficients.

This procedure was applied under three configurations: IMaX only, IMaX inserted in the ISLiD, and IMaX and ISLiD mounted on top of the telescope. In all cases, the vertical direction was selected as the $+Q$ orientation. For the case of IMaX alone, the demodulation

matrix obtained was (for camera 1 using vertical linear polarization)

$$\mathbf{D}_{\text{IMaX}} = \begin{Bmatrix} +0.25 & +0.25 & +0.25 & +0.25 \\ +0.41 & +0.41 & -0.43 & -0.36 \\ +0.41 & -0.56 & -0.43 & +0.57 \\ -0.58 & +0.59 & -0.39 & +0.40 \end{Bmatrix} \tag{8}$$

with typical errors of ± 0.01 in each of the coefficients (estimated from calibrations made on different days and in different places). Camera 2 (horizontal linear polarization) has a similar demodulation matrix with all signs in the D_{ij}, $i = 2, 3, 4$ terms exchanged. The efficiencies in this case were $\epsilon_{Q,U,V} = 0.62, 0.51, 0.50$, again above the requirement level. After insertion into the ISLiD and the telescope, the measured demodulation matrix was

$$\mathbf{D}_{Sunrise} = \begin{Bmatrix} +0.25 & +0.25 & +0.25 & +0.25 \\ +0.45 & +0.37 & -0.37 & -0.36 \\ +0.68 & -0.80 & +0.12 & -0.04 \\ -0.07 & +0.17 & +0.58 & -0.68 \end{Bmatrix} \tag{9}$$

with typical errors now of ± 0.02 in each of the coefficients. The corresponding efficiencies are: $\epsilon_{Q,U,V} = 0.64, 0.47, 0.54$, which still fulfil the original requirements but show an imbalance between the Q and U efficiencies which translates into a S/N 1.4 times better in the former Stokes parameter. The differences between $\mathbf{D}_{\text{IMaX}}$ and $\mathbf{D}_{Sunrise}$ can be ascribed to the folding mirrors present in the telescope (M3 and M4) and the ISLiD (five in total; see Gandorfer *et al.*, 2010). Note that $\mathbf{D}_{Sunrise}$ shows that both I and Q are evenly distributed among the four modulation states $[I_1, I_2, I_3, I_4]$. However, U is measured mostly in $[I_1, I_2]$ and V in $[I_3, I_4]$. As the number of accumulations is finally of the order of three to six, this difference is not likely to generate any systematic effect, but it is convenient to keep it in mind.

The matrix $\mathbf{D}_{Sunrise}$ was measured at ESRANGE while the LCVRs were at the nominal temperature of 35°C. As mentioned before, these nominal temperatures were never reached during science operations. The LCVRs mounting showed a fluctuating temperature in the telemetry (according to the daily variation) in the range $[29, 31]$°C. In order to account for this temperature difference, we have used the model mentioned in Section 3.2 to generate an additive correction to the involved Mueller matrices and inferred a flight demodulation matrix of

$$\mathbf{D}_{\text{flight}} = \begin{Bmatrix} +0.25 & +0.24 & +0.26 & +0.25 \\ +0.46 & +0.36 & -0.38 & -0.34 \\ +0.68 & -0.83 & +0.10 & +0.01 \\ -0.02 & +0.14 & +0.57 & -0.69 \end{Bmatrix} \tag{10}$$

with similar efficiencies. The differences between applying matrix $\mathbf{D}_{Sunrise}$ or $\mathbf{D}_{\text{flight}}$ is that the estimated residual cross-talk term $V \to U$ is reduced from 6% to 2%, respectively (see Section 9.2).

8.4. Spectroscopic Calibration

The spectroscopic characterization of the instrument included two different aspects. First, it had to provide the voltages under which the spectral line of interest should be found. Second, it should validate the instrument's spectral function expected for an etalon with the
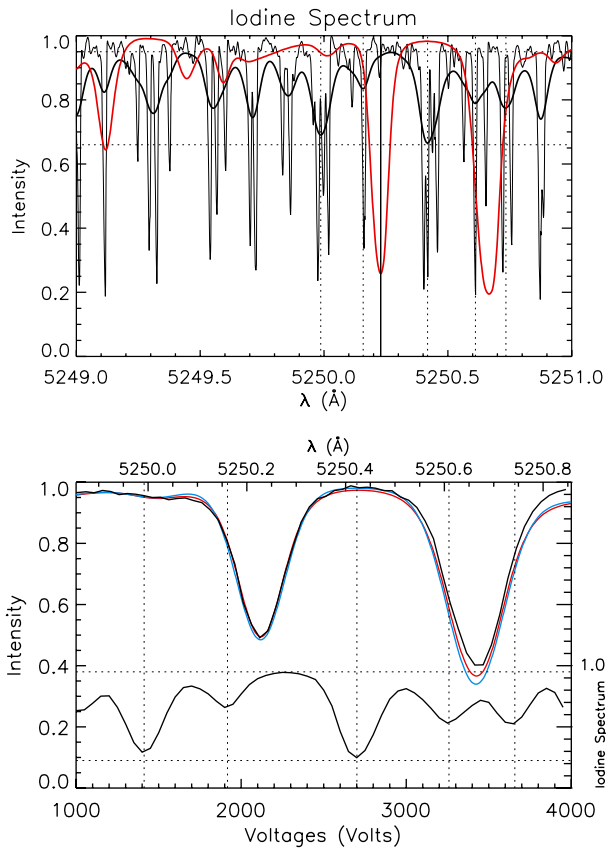
Figure 15 Top panel: The theoretical iodine spectrum is shown as thin solid line. The same spectrum after convolution with the IMaX theoretical profile is plotted as thick solid line. The red line represents the solar spectrum. The vertical solid line indicates the expected wavelength of the spectral line for the flight day. The dotted vertical lines mark the selected iodine blended spectral features used for wavelength calibration. Bottom panel: The black line on top is the solar spectrum as observed by IMaX at ESRANGE. The red line corresponds to the FTS spectrum convolved with the IMaX spectral point spread function. The blue line is the FTS spectrum convolved with an 85 mÅ FWHM Gaussian. Bottom part (right axis label): observed iodine spectrum by IMaX during the calibration phase at INTA. This curve has to be compared with that predicted from the theoretical iodine spectrum shown by the thick solid line in the top panel. The vertical dotted line represents the blended iodine spectral features identified for the calibrations. The horizontal dotted lines are given as estimates of the detected intensity fluctuations.

properties given in Table 4 and thus establish the effective resolution. As there was no option to feed the instrument with solar light during the AIV phase at INTA, the decision was taken to illuminate the instrument using an iodine (I_2) cell. Iodine cells have been extensively used for absolute spectral calibration of spectrometers (Gerstenkorn and Luc, 1978). They provide a wealth of thin spectral lines that can be used to establish a stable wavelength reference scale. Figure 14 (bottom panel) shows the iodine cell at the IMaX entrance during the AIV calibration phase. The spectrum of I_2 in the wavelength region of interest is shown by the thin solid line in the top panel of Figure 15. These lines have intrinsic widths of a few milliangstroms that cannot be resolved by IMaX. However, the convolution of the iodine spectrum with the Airy function of the double pass etalon (see Figure 2) shows a blended

spectrum with intensity fluctuations as large as 30% (solid line in the same panel of Figure 15), which can be used to calibrate the instrument. Also shown is the solar spectrum (red line) given for reference. The vertical dotted lines mark the five blended iodine lines selected for the voltage/wavelength calibration. Applying voltages in the range of [0, 4000] V and illuminating IMaX with the iodine cell produced the spectrum shown in the bottom panel of Figure 15 (bottom part; refer to the y-axis on the right). The comparison of the voltages at which the reference blended lines of iodine are found provides the voltage/wavelength calibration of the instrument:

$$\lambda - \lambda_0 = a + b \cdot V = -0.701 + 0.000335 \cdot V \tag{11}$$

with $\lambda_0 = 5250.225$ Å; wavelengths are in Å and voltages in V. The a coefficient gives the distance to the nominal wavelength of the line (λ_0) when the etalon is at 0 V. This distance to the spectral line of interest changes depending on where on the solar surface the observations are being made.

Once the integration of the gondola, telescope, and PFI was completed, *Sunrise* was pointed at the Sun for a few hours (as allowed by the weather conditions), and a basic calibration of the instrument could be performed. In particular, light level tests and the first identification of the spectral line were carried out. Figure 15 (bottom panel) shows the observed spectrum that includes the two Fe I lines at 5250.2 Å and 5250.6 Å (solid black line). The top x-axis provides the wavelength calibration obtained for the applied voltages. In this case, the inferred a coefficient was -0.703 Å, while b stayed basically the same. The red line represents the convolution of the Fourier transform spectroscopy (FTS) spectrum with the instrument profile from Figure 2, which produces a very satisfactory comparison. The spectral function used for the convolution has a range of 4 Å. Using such a long range can complicate the inversions of the data. In order to provide a simpler description of the spectral properties of IMaX, various Gaussians have been used to convolve the FTS data until a satisfactory agreement with the observed spectrum in ESRANGE is obtained. The blue line corresponds to a case where an 85 mÅ FWHM Gaussian has been used. Thus, even if the FWHM of the Airy function of the double etalon pass is of 65 mÅ, the effective resolution of the instrument, including spectral stray light from the side lobes, is degraded to 85 mÅ.

While the voltages needed to map the IMaX spectral line according to this calibration are in the range of [1800, 2400] V and of 2774 V for the continuum point (at $+0.227$ Å from line centre), the actual voltages used during the flight were higher, as the ambient temperatures never reached the expected values (those used for the calibrations). An automatic procedure was implemented in the instrument software that applies voltages from 1000 to 3000 V every 100 V and automatically finds the voltage for the intensity minimum. A parabolic fit around this minimum value provides an updated a coefficient. The values of this coefficient obtained during the flight were around -0.783 Å, *i.e.*, shifted 80 mÅ bluewards. Given the temperature sensitivity of this etalon (see Table 4), we deduce that it was 3.2°C cooler than when the calibrations were made on ground. This is a reasonable number, as the environment "seen" by the etalon was 5°C cooler, showing how effective the radiative coupling between the etalon and the surroundings was in the instrument. The flight voltages were on average higher, in the [2100, 2700] V range for sampling the spectral line and at 3010 V for the continuum point.

The automated procedure was used every time an observing run was started, allowing identification of the correct voltages to be used at the current *Sunrise* pointing. Due to solar rotation, the values of the a coefficient varied in the range -0.7830 ± 0.0325 Å.

8.5. Photon Budget

The number of photons, S, reaching the IMaX detectors is given by

$$S = N_\odot \phi^2 \Delta\lambda \, A_D \tau \, t_{ex}, \tag{12}$$

where $N_\odot$ is the number of photons coming from the Sun at 525 nm per unit time, area, solid angle, and wavelength interval. The solar specific intensity translates into $N_\odot = 9.2 \cdot 10^{17}$ photons s^{-1} cm^{-2} sr^{-1} Å^{-1}. ϕ^2 represents the subtended angular area of the detector pixels on the plane of the sky. $\Delta\lambda$ is the wavelength interval falling in one pixel and can be assimilated to the spectral resolution of the instrument $\delta\lambda$ (85 mÅ). A_D is the effective collecting area of the telescope and t_{ex} the exposure time of the individual frames as given in Table 1. $\tau = \tau_{Sunrise}\tau_{IMaX}$ stands for the transmission of the complete system, by far the most uncertain factor in this equation. While no precise measurements are available, estimates of the *Sunrise* global transmission (including four telescope mirrors, four ISLiD mirrors, five ISLiD lenses, and three ISLiD wavelength dichroics) suggest $\tau_{Sunrise} = 0.33$. The transmission of IMaX was also not accurately measured because of the inherent difficulties of such a measurement, but we estimate it to be $\tau_{IMaX} = 0.13$. This transmission includes three mirrors, nine lenses, two LCVRs, one pre-filter, one polarizing beamsplitter, and the four windows of the etalon together with the two passes on the etalon itself. These two passes are assumed to have a bandpass mismatch, resulting in a transmission reduction of 70% averaged over the entire surface. With these estimates, the global transmission of the system is $\tau = 0.043$. The photon flux can thus be estimated to be

$$S = 3.27 \cdot 10^5 \text{ photons pixel}^{-1}. \tag{13}$$

The detectors have a quantum efficiency of $Q = 25\%$, which results in a number of detected electrons of

$$S_e = QS = 8.1 \cdot 10^4 \text{ e}^- \text{ pixel}^{-1} \tag{14}$$

that fill 47% of the full well.[5] This predicts a count level of 1925 counts per single exposure (at continuum wavelengths), which is slightly higher than the observed count level of 1500 – 1600 counts (DC offset and dark current amounts to 60 digital units typically; see Table 5). We ascribe this small discrepancy to a slightly smaller overall transmission than the predicted value (τ of 0.034 instead of 0.043). Photon noise and readout noise add quadratically to produce $\sigma_e = 289$ e$^-$ pixel^{-1} and, thus, the signal-to-noise ratio of a single exposure was expected to be (for the estimated transmission) s/n $= S_e/\sigma_e = 280$. Now, using Equation (4), one can see that, in order to achieve the final value of S/N $\approx 10^3$ (700 per camera), we need to accumulate six frames in each of the modulation states. As the photon levels were slightly lower than estimated, the S/N of the accumulated frames at continuum wavelength in IMaX is indeed a bit lower than the expected 10^3 level. However, values near 900 are routinely measured in the reduced data.

9. Observing Modes and Data Analysis

During the 2009 flight, *Sunrise* observations in time-line (automated) mode included a calibration run before and after the planned scientific observations. These calibrations were

---

[5]This number has to be compared with the 10^7 photoelectrons for 1 G of sensitivity requirement introduced early in the paper.

Table 6 Observing modes of IMaX used during the 2009 flight

Observing mode	N_λ	N_p	N_A	Duration s	S/N	Line samples (mÅ)	Continuum (mÅ)
V5-6	5	4	6	33	1000	$-80, -40, +40, +80$	$+227$
V5-3	5	4	3	18	740	$-80, -40, +40, +80$	$+227$
V3-6	3	4	6	20	1000	$-60, +60$	$+227$
L3-2	3	2	2	8	1000	$-60, +60$	$+227$
L12-2	12	2	2	31	1000	-192.5 to $+192.5$ each 35	$+192.5$

done at disk centre, independently of the actual scientific pointing. They consisted of both flat-fielding series, with the telescope moving in circles of 100 arcsec radius around disk centre, and imaging series for IMaX PD calibrations, with the tracking re-enabled. IMaX was flat-fielded using the same observing mode (see next section) as that used in the following scientific run. In each flat-field series, 50 cycles of images (at each N_λ position and N_p modulation state) were acquired in time-line mode. After the scientific flat-fielding, the etalon was set to the continuum wavelength point and 50 PD flat-field images were recorded (with $N_\mathrm{A} = 6$). Once the telescope was stopped and the CWS locked at disk centre, 30 frames (again, at continuum wavelengths only and with $N_\mathrm{A} = 6$) were acquired, from which the system point spread function (PSF) can be inferred. IMaX dark current frames were taken in accordance with the CWS calibrations that commanded the dark current mask at F2.

9.1. IMaX Observing Modes

A number of observing modes are implemented in IMaX for its scientific operations. The modes differ in the number of wavelengths observed, in the number of accumulations used, and in the number of polarization states being obtained. The etalon is always set to a given wavelength position, and the polarizations are cycled N_A times. The total time of one cycle in each observing mode is thus $N_\mathrm{A} N_\mathrm{p} N_\lambda t_\mathrm{ex}$, plus a number of extra frames that are taken while the etalon is tuning to successive wavelength points, which are discarded later. As already discussed before, and shown in Table 4, the tuning constant of LiNbO$_3$ etalons requires several hundredths of a millisecond in order to tune a typical wavelength jump of $40 - 80$ mÅ. Thus, typically, IMaX discarded two or three frames every time the etalon was being tuned to a consecutive wavelength, thus adding an amount of $(2 - 3)N_\lambda t_\mathrm{ex}$ to the time given above. N_A is typically targeted to the required S/N of 1000, although observing modes with smaller signal-to-noise ratios, but offering faster cadences, are also implemented. The number of polarizations is either four, for the full Stokes vector mode, or two for the case of longitudinal observations only (including Stokes I and V). Table 6 lists all the observing modes used during the 2009 flight. The labels code the mode type (V for vector and L for longitudinal) followed by N_λ and, after a hyphen, N_A. The most commonly used observing mode was V5-6. The continuum point used in most of the observing modes (with the exception of L12-2) was set as the midpoint, in Stokes V profiles of network points, between the 5250.2 and 5250.6 Å lines.

We note that longitudinal observing modes are implemented in IMaX as if they were using four modulation states (as in vector modes). So L-modes are given in IMaX data as groups of four sets corresponding to $I_{1,2,3,4} \propto [I + V, I - V, I + V, I - V]$. The demodulation matrices for the L-modes should then be prepared accordingly and have 4×4 dimensions (as for the V-modes).

9.2. Data Reduction

Before data reduction starts for a given observing run (identified with an IMaX observing sequence number), several steps must be performed. The presence of interference fringes from some of the optical elements (the polarizing beamsplitter and the Barr pre-filter) together with some dust particles in optical elements near focal planes has considerably complicated the data reduction process. The presence of these unwanted patterns in the data was anticipated, but the fact that they drifted slowly following the thermal (diurnal) temperature changes of the instrument has forced us to always use the closest flat-field data set that is available. These diurnal temperature fluctuations were as large as 3°C as measured in some of the optical element mountings. Additionally, the interference fringes do not remain the same as the etalon is tuned to different voltages. The exact reason for this is unclear, but we are certain that the etalon, which is close to a pupil plane, slightly changes the incidence angle of the rays and modifies the fringe pattern for the various voltages used. The following steps must be performed before a proper data reduction can start.

1. The closest flat-field run and PD set (including observations and PD flats) must be identified. The closest dark frames must also be selected (although dark levels remained fairly constant throughout the flight).

2. A PD calibration consisting of inferring the instrument PSF as described by a set of 45 Zernike coefficients must be done. A detailed description of the PD inversion technique used here can be found in Paxman *et al.* (1996) and references therein. The retrieval of the system aberrations in every frame of the calibration set (a total of the 30 realizations of PD-pairs) is performed by applying PD inversions independently in 10×10 overlapped patches of 128×128 pixels. Since we have detected negligible anisoplanatism along the whole FOV, the Zernike coefficients retrieved from all patches in all the different realizations are then averaged to describe a mean wavefront and its corresponding PSF (Vargas Domínguez, 2009).

3. Next, a valid mean dark current and flat-field frames are generated for each of the $N_\lambda \times N_p$ states and for each camera by simple averaging the individual realizations (typically 50).

4. The above generated flats are affected by intensity fluctuations produced by the collimated configuration used for the etalon. These fluctuations must not be included in the subsequent correction of real data and so must be removed (*i.e.*, accounting for the blueshift effect in the flat-field data is necessary). The envisioned process leaves basically untouched the intensity fluctuations due to interference fringes, dust particles, illumination gradients, *etc.*, so that they are corrected from the real data after flat-field division. The main output from this procedure is the blueshift-corrected, flat-field frames at each wavelength and polarization state. This procedure also generates two additional important results. First, it calibrates the *a* coefficient (see Section 8.4) that corresponds to the actual pointing during the flat-field observations (in case they were not made exactly at disk centre). Second, it generates a set of coefficients for a surface fit to a third-degree polynomial that describes the blueshift over the FOV. These coefficients are later used for the pixel-to-pixel wavelength calibration.

5. Once these flat-fields are produced, they are applied to the images of the corresponding observing sequence that is farthest in time from the moment when they were acquired (and that will be more affected by the thermal drift of fringes and dust particles). The mean power spectrum of this sequence is used to define a mask in the Fourier domain providing the frequency ranges where residuals from the interference fringes are found. This mask will be applied to the power spectrum of every single image in the observing sequence, and the signal at the boundaries of the masked areas will be interpolated so

that a specific weighting function describing the excess of power within these areas can be constructed. This function, specific for every image, is finally used to filter out the excess of signal in the real and imaginary parts separately.

6. The same set of images used to derive the mask above serves to generate an additional mask (but now in the measurement domain) that marks the position of dust particles in the frames. These positions will be replaced by interpolating the signal at their boundaries, alleviating the effect of the particles. Note again that the original flat-field is unable to fully account for them due to their changing position as dictated by thermal drifts during the flight.

Early in the process, when producing the averaged darks and uncorrected flat-fields, the 936×936 central pixels of every image are extracted in order to eliminate the field stop used by the instrument at F4 as part of the strategy to reduce instrument stray light. Therefore, all subsequent images have these dimensions. After all this preliminary information has been created for a given observing sequence (containing a number of cycles, each one with $N_\lambda \times N_p$ images), the data reduction process can proceed. The steps below are followed.

1. The N_λ wavelengths and N_p states of a given cycle are dark subtracted, flat-fielded with the images resulting from step 4 above, and corrected for the pre-filter transmission curve (known from laboratory calibrations).
2. The masks from steps 5 and 6 above are used to filter out the residual excess power due to interference fringes in the Fourier domain and the dust particles residuals in the measurement domain.
3. The data are reconstructed using the PSF deduced from PD in step 2 above (whose Fourier transform is $S(s)$ with s the 2D spatial frequency of modulus s) and a modified Wiener optimum filter (from that originally proposed in 1971). This modification is implemented in order to avoid over-restoration in the high frequency domain and introduces a regularization parameter k. Specifically, the reconstructed images are obtained after computing the inverse Fourier transform of the product of the Fourier transform of the image, $I(s)$, times $\Phi(s)$ defined as

$$\Phi(s) = \frac{|I(s)|^2 - |N(s)|^2}{|I(s)|^2} \frac{S^*(s)}{|S(s)|^2 + k(s/s_c)}. \tag{15}$$

$N(s)$ is the spectrum of the noise assumed here to be constant and evaluated from the power observed near the cutoff frequency s_c. The regularization parameter $k = 0.005$ is allowed to obtain contrast values of the restored granulation similar to those obtained in ground-based short exposure images while reducing the amplification of the noise at high frequencies.

The PD restoration technique is applied in the Fourier domain that requires a FOV apodization, which effectively reduces the IMaX FOV in all of its sides by typically 30 pixels (thus leaving a usable FOV of 876×876 pixels or 48×48 arcsec). The output from this step consists of both the non-reconstructed (Level 1) and reconstructed (Level 2) data. Both data sets are treated similarly in the subsequent steps of the data reduction process.

4. Data are demodulated using the $\mathbf{D}_{\text{flight}}$ matrix.
5. The residual cross-talk with intensity is estimated at the continuum frame and corrected for in all observed wavelengths.
6. The intensities of the two cameras are equalized, the relative displacement between the two found, and the data from the two cameras added to reduce jittering-induced cross-talk (which in this case corresponds, to first order, to some gradient along the direction

of the motion of the intensity frame that is transmitted to the polarization signals; see Lites, 1987). Similarly, the data from the two cameras are subtracted to produce the corresponding jittering-induced polarization image.

7. The resulting frames from merging the two cameras are analysed locally (boxes of 52 × 52 pixels or 2.86 arcsec square) to ensure that global linear trends in the polarization observed in continuum are not present and if so, removed. Similarly if local correlations with the jittering-induced polarization images produced in the previous step are found, they are subtracted out.

8. Finally, residual cross-talk from Stokes V to Q and U is sought (by correlating the corresponding frames), and if statistically significant amounts of V are found, a correction is applied. It is in this step where using the matrix of Equation (10) instead of that in Equation (9) is noticeably better.

The output of both Level 1 and Level 2 corrected data are finally written in Flexible Image Transport System (FITS) format.

9.3. Sample Data and Calibration

IMaX data reduced as explained in the previous section correspond to the Stokes profiles sampled at various wavelength positions. At the time of writing this paper, this procedure has been applied to several V5-6 (see Table 6) runs obtained on 9 June 2009 (the launch was on the morning of the 8th). It has also been preliminarily applied to other data taken during the flight including the very last day, a few hours before the balloon cut-off. These data indicate that the instrument performance was basically the same all along the flight without any noticeable degradation. By selecting regions with no clear signs of polarization signals on the reduced data, an estimate of the final S/N achieved in the individual wavelengths has been made. For non-reconstructed data, values between $800 - 1100$ are obtained, and the noise changes in random ways from pixel to pixel. We take this as evidence for photon-noise dominated data. However, the situation for the PD-reconstructed data is different. The reconstruction process amplifies all frequencies but emphasizes more the power at intermediate and high frequencies. This results in an increased noise level. Estimates made over the same regions as those made for non-reconstructed data show noise levels a factor $2.5 - 3$ times higher after the reconstruction process. Of course, the polarization signals themselves are also higher, but typically by a factor two, resulting in a polarization S/N that is slightly smaller in the reconstructed data. But the S/N, which is typically referred to the continuum level, does not benefit from the increased polarization signals and results in values of $300 - 400$. Additionally, the noise develops a spatial pattern of a few (two or three) pixels in size that originates from the reconstruction process at high frequencies. The free parameters (controlling the enhancement of high frequency power) used in the reconstruction, including the regularization parameter k, were fine-tuned to avoid clear signs of over-restoration in the polarization signals (as evidenced by the appearance of opposite polarity signals surrounding field concentrations), but still producing granular contrasts as found for the PD calibration data (which often reaches $14 - 15\%$ at disk centre; non-reconstructed data show contrasts in the range of $8 - 8.5\%$).

To display the data and fully appreciate its quality, a basic calibration has been performed. Stokes I samples (four inside the line plus continuum) were fitted to a Gaussian providing the central wavelength, the line centre intensity, and the line FWHM. The central wavelength, after correction for blueshift, provides the LOS Doppler velocity. Longitudinal and transverse magnetograms have been constructed by averaging the four samples of Q_i, U_i, and V_i inside the line. For Stokes V the two red wavelength points had their sign

changed to avoid cancellation. In the case of Q and U, the average was done for $\sqrt{Q^2 + U^2}$. Specifically, the following samples were created from the data:

$$V_{\mathrm{s}} = \frac{1}{4} \sum_{i=1}^{4} a_i V_i \quad \text{and} \quad L_{\mathrm{s}} = \frac{1}{4} \sum_{i=1}^{4} \sqrt{Q_i^2 + U_i^2}, \tag{16}$$

with the $\bar{a}$ vector being $[1, 1, -1, -1]$. Note that the V_{s} and L_{s} samples have half the noise of any individual wavelength. While these samples provide polarization signals, they can be transformed into equivalent gauss (or $\mathrm{Mx\,cm^{-2}}$) units in order to provide a better comparison with similar instruments. To this end, the Fe I line at 5250.2 has been synthesized in the Holweger and Mueller (1974) quiet-Sun model using various magnetic configurations. For the longitudinal calibration, a set of field strengths varying between 1 and 2500 G aligned with the LOS was used. The same set of field strengths is used for the transverse field calibration, but with an inclination of 90° with respect to the LOS and an azimuth of 0°. In both cases, the resulting profiles are convolved with the IMaX spectral profile of Figure 2 and sampled at the same four wavelengths as the real data. A linear least-squares fit is made in the range of $[0, 400]$ G, where the calibration curve still shows a clear linear character, to provide[6]

$$B_{\mathrm{L}}(\mathrm{G}) = 4759 \frac{V_{\mathrm{s}}}{I_{\mathrm{c}}}, \quad \text{and} \quad B_{\mathrm{T}}(\mathrm{G}) = 2526 \sqrt{\frac{L_{\mathrm{s}}}{I_{\mathrm{c}}}}, \tag{17}$$

where I_{c} is the continuum intensity at the observed pixel. These equations allow one to transform (under the assumptions listed above) polarization fractions into equivalent gauss values. A 10^{-3} noise level corresponds to a 4.8 G longitudinal field sensitivity and to an 80 G transverse field sensitivity. These are typical sensitivities of non-reconstructed magnetograms. For reconstructed data (S/N $\approx$ 350), the sensitivities are 14 G and 135 G, respectively. But note that these numbers heavily depend on the atmospheric model being assumed. This is particularly true for the extremely temperature-sensitive line used by IMaX. For example, if use is made of a network atmospheric model (Solanki, 1987), the constants in Equation (17) change to 11 970 G and 3354 G for the longitudinal and transverse cases, respectively. Additionally, the line intensity minimum changes from 0.5 to 0.8, reflecting the smaller absorption produced in a hotter atmosphere for this line. Thus, a kilogauss field produces a signal of 0.21 in V_{s} for the quiet-Sun model but of only 0.08 for the network one. For the present case, and due to the extremely quiet nature of the observed regions, we consider it more adequate to use the constants in Equation (17) and keep in mind that they underestimate the equivalent fields (or flux densities) by a factor two, or more, in network concentrations. Note also that if one simply multiplies the V_{s} and L_{s} frames by these constants, the effect of the blueshift of the line over the FOV is not corrected. In order to account for this effect, a calibration similar to that described above, but with the samples shifted to the blue by known amounts, was made. This allows one to understand how these constants change within the IMaX FOV and produce a calibration frame (instead of a calibration constant) that, when multiplied to the polarization samples, fully corrects the blueshift effect. The magnetograms presented in this section were transformed into equivalent gauss values with these calibration frames and are, therefore, free from the blueshift over the FOV.

---

[6]The minimum number of photoelectrons for a 1 G detection in the introduction comes directly from the coefficients in Equation (17).

Figure 16 Power spectrum of an IMaX continuum image after PSF restoration in the horizontal (*x*-section) and vertical direction (*y*-section). The horizontal lines represent the estimates of the noise level in the data.
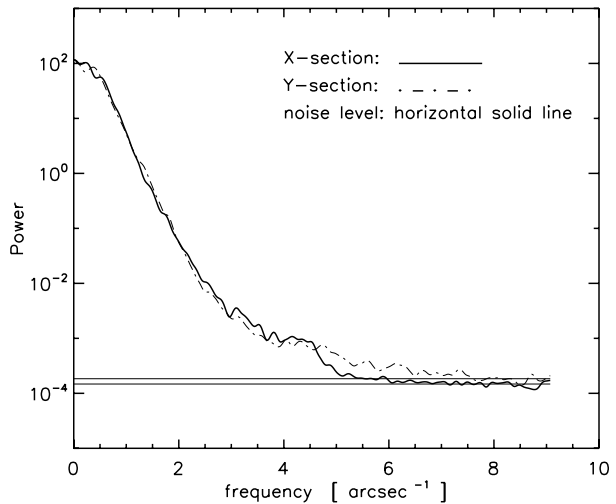

Figure 17 shows an example of IMaX data after the reduction process of Section 9.2 and calibrated as explained above. From top to bottom and left to right, we show a continuum intensity frame, a longitudinal magnetogram, the same longitudinal magnetogram with no reconstruction process, the corresponding transverse magnetogram (non-reconstructed), the LOS velocity frame, and the line centre intensity map. The continuum intensity frame has an rms contrast of 12.5%. The effect of image apodization can be seen near the boundaries of the image. Two cuts of the power spectrum of this frame in orthogonal directions are shown in Figure 16. If we estimate the noise level as marked by the horizontal lines, the image power reaches the noise at frequencies corresponding to spatial scales of $0.15 - 0.18$ arcsec. This demonstrates the spatial resolution reached by *Sunrise*/IMaX. We stress that, by construction, the spatial resolution is the same for continuum images, magnetograms, Dopplergrams, or for any line parameters inferred from the spectral samples. The two longitudinal magnetograms are provided to allow a comparison of the effects of image reconstruction in them. The smaller sizes that are associated to the field concentrations in the reconstructed data show the benefits of the process. A more evident mixed polarity nature of the field distribution is also noticeable. The downside is represented by the noise pattern that is stronger in the reconstructed data. The scaling of the longitudinal fields (± 40 G) corresponds to a polarization level $8 \cdot 10^{-3}$, whereas the noise of this magnetogram is $5 \cdot 10^{-4}$ (non-reconstructed; for the reconstructed frame it is $1.5 \cdot 10^{-3}$) as benefited from the average over the four spectral points. The transverse field image is represented in negative numbers to provide a better visibility of the horizontal fields. This trick follows the work of Lites *et al*. (2008), who found internetwork horizontal signals similar to those shown here. The equivalent gauss levels found in this transverse map are about 180 G before reconstruction and 260 G after the reconstruction process. Given the noise level of the latter data, the reconstructed transverse magnetograms have a usability limited to the strongest concentrations. The transverse field image shows evident signatures that resemble the solar granulation. While some image jittering-induced cross-talk remains in the data, typically at the $1 - 2 \cdot 10^{-3}$ level over intergranular lanes, the reason for it being so prominent here is different. Noise in the transverse data produces a positively defined veil of 80 G from where real signals have to stand out. When no signals are present above this level, the $1/\sqrt{I_c}$ component of Equation (17) fluctuates according to the granular pattern and makes it thus prominent. The two last plots are derived from the Gaussian fits to the Stokes *I* profiles. The Doppler image has an rms velocity
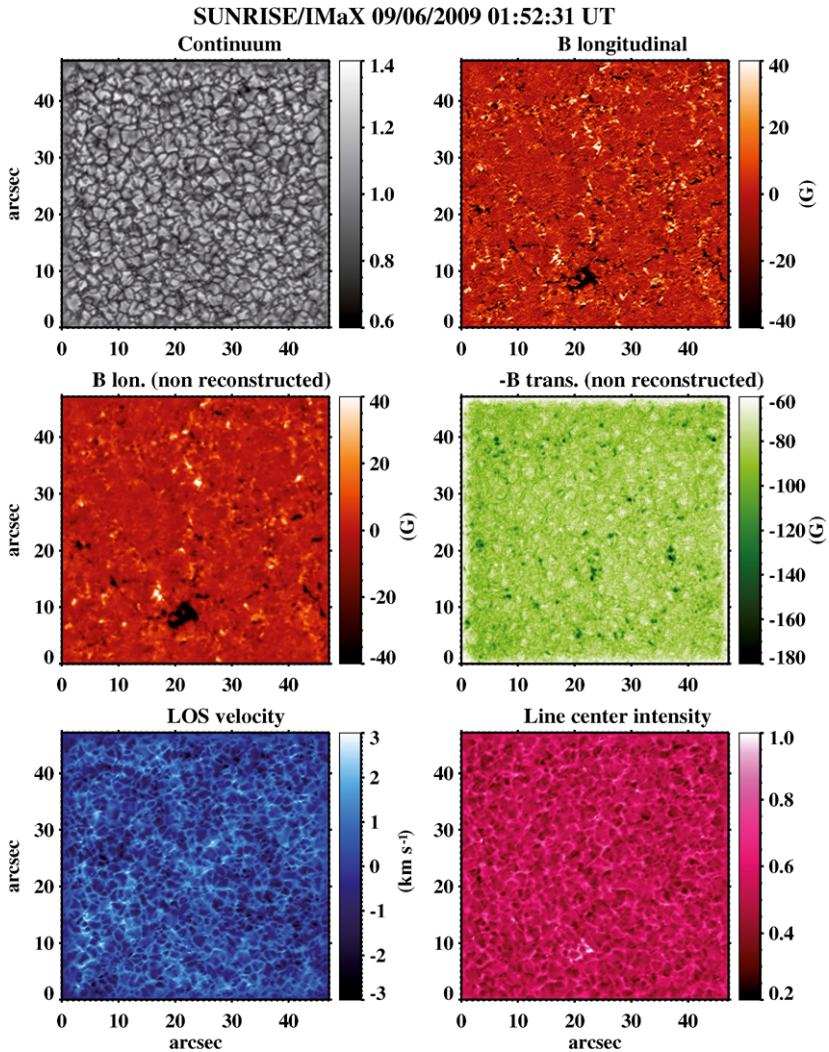
Figure 17 Sample data taken by *Sunrise*/IMaX on the early morning of 9 June 2009, a few hours after the launch. See text for details.

fluctuation of 0.73 km s^{-1}. Extreme velocities (both upflows and downflows) have a magnitude of 3.5 km s^{-1}. The statistical errors (from the Gaussian fit) of the Doppler velocities are in the range of 0.005 – 0.01 km s^{-1} for the non-reconstructed data and of 0.02 – 0.04 km s^{-1} for the reconstructed ones. However, sometimes the simple Gaussian fit fails in the presence of strong network signals as a result of the combination of the Zeeman broadening and the line weakening due to the temperature excess. Under these circumstances, four points cannot provide a good Gaussian fit (although velocities from an inversion code that also uses Stokes *V* are accurate). The line centre intensity fluctuates in the range between 0.2, as found in small-scale granular structures, to 0.9 in the strongest network regions near the bottom of the frame. The mean value of this magnitude is 0.5, as predicted by the Holweger – Mueller model and the IMaX spectral resolution.

10. Conclusions

The IMaX instrument that flew in the *Sunrise* stratospheric balloon in June 2009 for almost six days has been presented. The design, calibration, and integration phases have been discussed in detail. No degradation of the instrument performance has been observed in the analysed data so far. After its recovery and translation to INTA facilities, the instrument was switched on and images were acquired at nominal conditions with only some signs of optical misalignment. The consumption of the instrument was at nominal values, including the HVPS, showing that the LiNbO$_3$ etalon is acting as a capacitor and suffered no structural damage. Although careful spectral and polarimetric end-to-end tests have not been performed yet, the instrument seems to have survived the polar flight in rather good condition.

The results presented here clearly show that IMaX/*Sunrise* data will allow solar magnetic and velocity fields to be studied with a resolution of $0.15 - 0.18$ arcsec for periods of times of around 30 min in the different observing modes used by the instrument. Magnetic sensitivities are well below 10 G for longitudinal fields and 100 G for transverse fields. The *Sunrise* telescope was pointed at various places in the Sun, including a number of intermediate positions between disk centre and the solar limb. These data sets of unprecedented quality will provide a wealth of information about the quiet-Sun magnetic fields, dynamics, and interaction with the solar granulation.

References

Álvarez-Herrero, A., Belenguer, T., Pastor, C., González, L., Heredero, R.L., Ramos, G., *et al.*: 2006a, In: Mather, J.C., MacEwen, H.A., de Graauw, M.W.M. (eds.) *Space Telescopes and Instrumentation I: Optical, Infrared, and Millimeter*, *Proc. SPIE* **6265**, 62654C.

Álvarez-Herrero, A., Belenguer, T., Pastor, C., Heredero, R.L., Ramos, G., Martínez Pillet, V., Bonet Navarro, J.A.: 2006b, In: Mather, J.C., MacEwen, H.A., de Graauw, M.W.M. (eds.) *Space Telescopes and Instrumentation I: Optical, Infrared, and Millimeter*, *Proc. SPIE* **6265**, 62652G.

Arkwright, J., Underhill, I., Pereira, N., Gross, M.: 2005, *Opt. Express* **13**, 2731.

Atherton, P.D., Reay, N.K., Ring, J., Hicks, T.R.: 1982, *Opt. Eng.* **20**, 806.

Barthol, P., Gandorfer, A., Solanki, S.K., Schüssler, M., Chares, B., Curdt, W., et al.: 2010, *Solar Phys.*, this issue. doi:10.1007/s11207-010-9662-9.

Bello González, N.: Kneer, F., 2008, *Astron. Astrophys.* **480**, 265.

Berkefeld, T., Schmidt, W., Soltau, D., Bell, A., Doerr, H.P., Feger, B., *et al.*: 2010, *Solar Phys.* doi:10.1007/s11207-010-9676-3.

Bernasconi, P., Rust, D., Eaton, H., Murphy, G.: 2000, In: Melugin, R.K., Roeser, H.-P. (eds.) *Airborne Telescope Systems*, *Proc. SPIE* **4014**, 214.

Brault, J.W., White, O.R.: 1971, *Astron. Astrophys.* **13**, 169.

Collados, M.: 2009, In: *Proc. 12th European Solar Physics Meeting*. http://espm.kis.uni-freiburg.de/, t_6-04.

Collados, M., Lagg, A., Díaz García, J.J., Hernández Suárez, E., López López, R., Paéz Mañá, E., Solanki, S.K.: 2007, In: Heinzel, P., Dorotovic, I., Rutten, R.J. (eds.) *The Physics of Chromospheric Plasmas*, *ASP Conf. Ser.* **368**, 611.

Del Toro Iniesta, J.C.: 2003, *Introduction to Spectropolarimetry*, Cambridge.

Del Toro Iniesta, J.C., Collados, M.: 2000, *Appl. Opt.* **39**, 1637.

Elmore, D.F., Lites, B.W., Tomczyk, S., Skumanich, A.P., Dunn, R.B., Schuenke, J.A., Streander, K.V., Leach, T.W., Chambellan, C.W., Hull, H.K.: 1992, In: Goldstein, D.H., Chipman, R.A. (eds.) *Polarization Analysis and Measurement*, *Proc. SPIE* **1746**, 22.

Gandorfer, A., Steiner, H.P., Povel, P., Aebersold, F., Egger, U., Feller, A., Gisler, D., Hagenbuch, S., Stenflo, J.O.: 2004, *Astron. Astrophys.* **422**, 703.

Gandorfer, A., Grauf, B., Barthol, P., Riethmüller, T.L., Solanki, S.K., Chares, B., *et al.*: 2010, *Solar Phys.*, this issue. doi:10.1007/s11207-010-9636-y.

Gary, G.A., Balasubramaniam, K.S., Sigwarth, M.: 2003, In: Keil, S.L., Avakyan, S.V. (eds.) *Innovative Telescopes and Instrumentation for Solar Astrophysics*, *Proc. SPIE* **4853**, 252.

Gerstenkorn, S., Luc, P.: 1978, *Atlas du Spectre d'Absorption de la Molecule d'Iode*, CNRS, Orsay.

Heredero, R.L., Uribe-Patarroyo, N., Belenguer, T., Ramos, G., Sánchez, A., Reina, M., Martínez Pillet, V., Álvarez-Herrero, A.: 2007, *Appl. Opt.* **46**, 689.

Holweger, H., Mueller, E.A.: 1974, *Solar Phys.* **39**, 19.

Kentischer, T.J., Schmidt, W., Sigwarth, M., Uexkuell, M.V.: 1998, *Astron. Astrophys.* **340**, 569.

Kosugi, T., Matsuzaki, K., Sakao, T., Shimizu, T., Sone, Y., Tachikawa, S., *et al.*: 2007, *Solar Phys.* **243**, 3.

Lites, B.W.: 1987, *Appl. Opt.* **26**, 3838.

Lites, B.W., Elmore, D.F., Streander, K.V.: 2001, In: Sigwarth, M. (ed.) *Advanced Solar Polarimetry – Theory, Observation, and Instrumentation*, *ASP Conf. Ser.* **236**, 33.

Lites, B.W., Scharmer, G.B., Berger, T.E., Title, A.M.: 2004, *Solar Phys.* **221**, 65.

Lites, B.W., Kubo, M., Socas-Navarro, H., Berger, T., Frank, Z., Shine, R., *et al.*: 2008, *Astrophys. J.* **672**, 1237.

Martínez Pillet, V.: 2006, In: Marsden, R., Conroy, L. (eds.) *Proc. Second Solar Orbiter Workshop*, *ESA SP-641* (on CD-ROM).

Martínez Pillet, V., Collados, M., Sánchez Almeida, J., González, V., Cruz-Lopez, A., Manescau, A., *et al.*: 1999, In: Rimmele, T.R., Balasubramaniam, K.S., Radick, R.R. (eds.) *High Resolution Solar Physics: Theory, Observations, and Techniques*, *ASP Conf. Ser.* **183**, 264.

Martínez Pillet, V., Bonet, J.A., Collados, M.V., Jochum, L., Mathew, S., Medina Trujillo, J.L., *et al.*: 2004, In: Mather, J.C. (ed.) *Optical, Infrared, and Millimeter Space Telescopes*, *Proc. SPIE* **5487**, 1152.

Noll, R.J.: 1976, *J. Opt. Soc. Am.* **66**, 207.

Orozco Suárez, D.: 2008, Diffraction-Limited Spectropolarimetry of Quiet-Sun Magnetic Fields, Ph.D. thesis, University of Granada.

Orozco Suárez, D., Bellot Rubio, L.R., Martínez Pillet, V., Bonet, J.A., Vargas Domínguez, S., *et al.*: 2010, *Astron. Astrophys.*, in press.

Paxman, R.G., Seldin, J.H., Loefdahl, M.G., Scharmer, G.B., Keller, C.U.: 1996, *Astrophys. J.* **466**, 1087.

Pietarila Graham, J., Danilovic, S., Schüssler, M.: 2009, *Astrophys. J.* **693**, 1728.

Puschmann, K.G., Kneer, F., Seelemann, T., Wittmann, A.D.: 2006, *Astron. Astrophys.* **451**, 1151.

Rimmele, T., Keil, S., Wagner, J., Team, A.T.S.T.: 2009, In: *Proc. 12th European Solar Physics Meeting*, http://espm.kis.uni-freiburg.de/, t_6-03.

Scharmer, G.: 2006, *Astron. Astrophys.* **447**, 1111.

Scharmer, G.: 2009, *Space Sci. Rev.* **144**, 229.

Scharmer, G.B., Narayan, G., Hillberg, T., de la Cruz Rodriguez, J., Löfdahl, M.G., Kiselman, D., Sütterlin, P., van Noort, M., Lagg, A.: 2008, *Astrophys. J. Lett.* **689**, 69.

Scherrer, P.H., Bogart, R.S., Bush, R.I., Hoeksema, J.T., Kosovichev, A.G., Schou, J., *et al.*: 1995, *Solar Phys.* **162**, 129.

Shimizu, T., Nagata, S., Tsuneta, S., Tarbell, T., Edwards, C., Shine, R., *et al.*: 2008, *Solar Phys.* **249**, 221.

Solanki, S.K.: 1987, Properties of Solar Magnetic Fluxtubes, Ph.D. thesis, ETH, Zürich.

van Noort, M.J., Rouppe van der Voort, L.H.M.: 2008, *Astron. Astrophys.* **489**, 429.

Vargas Domínguez, S.: 2009, High Resolution Study of Solar Active Regions through Phase Diversity Techniques, Ph.D. thesis, University of La Laguna.

Viticchié, B., Del Moro, D., Berrilli, F., Bellot Rubio, L., Tritschler, A.: 2009, *Astrophys. J. Lett.* **700**, 145.

von der Lühe, O., Kentischer, Th.J.: 2000, *Astron. Astrophys.* **146**, 499.

Vögler, A., Shelyag, S., Schüssler, M., Cattaneo, F., Emonet, T., Linde, T.: 2005, *Astron. Astrophys.* **429**, 335.